Formation of the active site structures during pyrolysis transformation of Fe-phthalocyanine into Fe-N$_x$-C electrocatalysts for the oxygen reduction reaction

Mohsin Muhyuddin [a], Enrico Berretti [b], Seyed Ariana Mirshokraee [a], Jacopo Orsilli [a], Roberto Lorenzi [a], Laura Capozzoli [b], Francesco D'Acapito [c], Eamonn Murphy [d], Shengyuan Guo [d], Plamen Atanassov [d], Alessandro Lavacchi [b], Carlo Santoro [a],*

[a] *Department of Materials Science, University of Milano-Bicocca, U5, Via Roberto Cozzi, 55, Milano 20125, Italy*
[b] *Istituto di Chimica Dei Composti OrganoMetallici (ICCOM), Consiglio Nazionale Delle Ricerche (CNR), Via Madonna Del Piano 10, Sesto Fiorentino, Firenze 50019, Italy*
[c] *CNR-IOM-OGG, c/o ESRF LISA CRG, Avenue des Martyrs 71, Grenole 38000, France*
[d] *Department of Chemical and Biomolecular Engineering, University of California, Irvine, CA 92697, United States*

ARTICLE INFO

ABSTRACT

Fe-N$_x$-C electrocatalysts for the oxygen reduction reaction are typically fabricated via pyrolysis. However, the pyrolysis process is poorly understood. Therefore, a systematic investigation was initiated to elucidate the effects of the pyrolysis conditions (atmosphere and temperature) on the evolution of active sites starting from iron phthalocyanine supported over carbon black. The atomic level dispersion of Fe-N$_x$ is sustained up to 600 °C and afterward, the growth of iron oxide nanoparticles is observed. Interestingly, the different X-ray absorption spectroscopy fingerprints acquired during in-situ and ex-situ experiments indicated the bonding of oxygen as a fifth ligand on the Fe sites when exposed to the open air. The ORR activities were analyzed in acidic and alkaline media. The best electrocatalytic activity was observed for the electrocatalysts pyrolyzed at 600 °C. Above this temperature, a reduction in the activity was observed. Surface-to-reactivity analysis was carried out identifying the relationship between surface chemistry/morphology and electrocatalytic activity.

1. Introduction

Where unprecedented technological advancements are revolutionizing the human standards of living, the ever-increasing global population and industrial growth have brought a quandary for the contemporary era in which the depletion of fossil fuels and climatic dilemmas are flaring up several socio-economic crises. To mitigate such a looming scenario, the 'Hydrogen Economy' with a mandate of introducing hydrogen as a green and sustainable energy vector provides a ray of hope [1–4]. The most efficient way to produce hydrogen is via electrochemical water electrolyzers by employing renewable energy sources; the H$_2$ produced can be utilized afterward as a fuel in fuel cells (FCs) to produce electricity. FCs with their unparalleled capacity to continuously transform fuel into electricity without contributing to the global carbon footprint can be installed in both stationary and mobile applications [5–8]. Tremendous scientific interest in FCs has been devoted

but still, this technology has a critical bottleneck lying at the cathodic side of the system executing the oxygen reduction reaction (ORR) with sluggish kinetics and complicated pathways. The aforementioned issue is often addressed by deploying platinum-group metals (PGMs)-based ECs. This solution severely makes it difficult to sustain a wide diffusion of the FC devices, accounting their rarity and economic cost of the electrocatalysts they use. According to a recent estimation, PGM-based ECs in PEMFC account for approximately 56% of the total cost of FC stack, representingthe biggest obstacle in the mass-scale production of FCs [9,10]. Consequently, the pursuit to develop sustainable PGM-free ECs has acquired paramount importance to reach the marketization of FCs. As a result of a plethora of scientific endeavors in this regard, atomically dispersed metal-nitrogen-carbons (M-N$_x$-Cs) have been emerging as a reliable substitute for PGMs [5,8,9,11–18]. Such M-N$_x$-Cs can be fabricated using earth-abundant first-row transition metals (TMs) where metallic atoms in coordination with nitrogen (TM-N$_x$ with x = 2,

* Corresponding author.
  E-mail address: carlo.santoro@unimib.it (C. Santoro).

3,4) and embedded in carbon matrix bio-mimics the ORR capability of natural enzymes i.e. cytochrome-c-oxidase and hemoglobin [19,20]. This category of ECs shows important activity even more appreciated in operations in alkaline media that have recently gained interest with the development of stable anion exchange membranes (AEMs).

Different TMs i.e. Mn, Fe, Co, Ni, Cu, etc. have been exploited for the development of single-atom TM-N_x-C-based ECs. However, Fe remains as the TM of the choice owing to its suitable electronic structure and thermodynamic interaction with oxygen that synergistically contribute to the ORR and put Fe (having coordination with nitrogen) nearly at the apex of the volcano plot while fulfilling the Sabatier's principle [20–22]. Fe-N_x-Cs contain a multitude of active sites where atomically dispersed Fe-N_x (x = 2,3,4) and pyridinic nitrogen are usually considered to be the primary active site and secondary active site, respectively [10,23–27]. In fact, the former can ensure the tetra-electronic electro-reduction of oxygen as the final product whereas pyridinic nitrogen acts as a secondary site for the stepwise reduction of the undesired intermediate into the final product, which was previously generated as a result of bi-electronic ORR [23]. Moreover, Wu et al. have recently exhibited that when the Fe^{2+}/Fe^{3+} ratio is optimal on the EC surface, an appreciable kinetics of the ORR process can be achieved, particularly in alkaline media [28]. A huge variety of iron salts, nitrogen sources, macro-organic molecules and carbonaceous precursors can be utilized to develop Fe-N_x-Cs. However, pyrolysis is considered the only reliable methodology to induce favorable and robust active sites in Fe-N_x-Cs with atomic level homogeneity [29,30]. Pyrolysis is a thermal treatment that takes place in a controlled atmosphere without any involvement of oxygen. Despite being the most commonly practiced methodology for EC fabrication, pyrolysis itself is a poorly understood phenomenon that can be regarded as a "Black Box" [31,32]. The core rule of materials engineering discloses the fact that the process dictates the structure, which ultimately influences the performance; therefore, a systematic study of the pyrolysis process is crucial to enable the rational development of efficient Fe-N_x-C ECs.

Not long ago, Li and co-researchers encouraged the scientific community to gain a profound understanding of the evolutionary pathway of the single atom Fe(II)-N_4 site in Fe-N_x-Cs during pyrolysis [33]. Employing in-situ X-ray absorption spectroscopy (XAS), they systematically observed the gaseous phase transformation of precursors into particularly Fe(II)-N_4 active moieties above 600 °C after passing through different interim stages during pyrolysis. Moreover, while analyzing the influence of pyrolysis conditions on the ORR performance of cobalt–doped MOF–based carbon ECs, Cui et al. concluded that electrocatalytic activity is closely dependent on the pyrolysis temperature and applied heating ramp rate whereas dual–step pyrolysis can effectively improve ORR activity [34]. By the same token, Huang et al. initiated a systematic study to directly observe the chemical makeovers and morphological development of Fe-N_x-Cs during the pyrolysis-assisted transformation of nitrogen and carbon precursor (Nicarbazin) mixed with iron salt and amorphous silica (templating agent) by combining in-situ light synchrotron and ex-situ analytical methods [31]. In the succeeding study, Chen and the group gave new insight into the structural rearrangement taking place during the second pyrolysis of the same Fe-N_x-C EC after the removal of the silica template [32]. It was observed that the second pyrolysis results in the partial restoration of an amorphous phase, together with the formation of various nitrogen-carrying sites, eventually leading to the homogeneous dispersion of Fe-N_x at the atomic level without the formation of nanoparticles. In addition to the second heat treatment, switching the pyrolysis atmosphere can also influence the structural parameters of the Fe-N_x-C EC. Furthermore, Santori et al. clarified that change in the pyrolysis atmosphere not only affects the activity of the derived EC but also impacts its operational durability which correspondingly shifts as the pH of electrolytic media is altered [35]. Similarly, Zitolo and co-researchers disclosed the fact that despite having apparently identical active moieties, Fe-N_x-Cs pyrolyzed under different flowing atmospheres may have

different ORR activities due to modification in the basicity of N-groups that form during pyrolysis [36]. Moreover, in 2018, Kabir et al. studied the synthesis and performance relationship among nitrogen-based moieties present in the N-functionalized graphene towards ORR kinetics and reduction routes in acidic and alkaline conditions [37]. An in-depth examination of surface chemistry revealed that pyrolysis temperature decides the type and proportion of N-based moieties which contrarily dictate the ORR in the varying electrolytic conditions. Likewise, Vallejos-Burgos and coworkers pyrolyzed different phthalocyanines (Pc) such as cobalt Pc, copper (Pc) and Pc without any metallic substitution over the range of 550–1000 °C and analyzed the structural modifications [38]. Their study uncovered that the metallic coordination enhances the thermal durability of the Pc configuration in an inert atmosphere, however, in the oxidizing environment it causes gasification even well before the decomposition temperature. Not long ago, Oliveira reported the progress in the utilization of metal-N_4 chelates for ORR and then supported FePc over different carbon supports to fabricate EC for alkaline media [39]. Although the use of Pcs is not new in the FCs domain as Jasinski pioneered their employment for the cathode ECs in 1964 [40], their electrocatalytic activity is known to degrade over time because of demetallation or unwanted oxidation by ORR intermediates i. e. peroxides [41,42]. However, compositing the Pc molecules with carbon and giving them a heat treatment is considered an effective strategy to improve the working durability of the Pc-based ECs [41,43, 44].

Notwithstanding the important individual efforts to figure out the effect of pyrolysis conditions on the structural evaluation of Fe-N_x-Cs, a comprehensive understanding of pyrolysis is still missing. In addition to Fe-free (carbon or nitrogen-based sites) and Fe-N_x, several other Fe-based active sites are also formed at different stages of pyrolysis, influencing the overall ORR activity in a complex, not-always predictable way. The iron atom has many unoccupied d orbitals and therefore it forms various sorts of coordinations, geometrical arrangements and interfaces with nitrogen or neighboring atoms [23–25]. Such multitudinous moieties demonstrate varying activities and robustness during the ORR and therefore demand proper site engineering [45–47]. Previous research is primarily focused on the role of metal-free site structures or Fe-N_x-type moieties in ECs. Today, some process influences are still unresolved. Importantly, the influence of pyrolysis conditions in the nucleation, growth and transformation of such multitudinous active moieties that could ultimately impact the parameters of the electrochemical performance of single atom Fe-N_x-Cs is unclear. Therefore, a basic question arises: how can the surface chemistry and morphological aspects be correlated with the evolution and specification of Fe-based moieties in a broader spectrum? Such curiosities constitute a research hotspot of utmost significance to gain an insightful and comprehensive understanding of Fe-N_x-Cs development via pyrolysis that would help reveal the true connections among processing, structure, and performance factors.

Taking note of the abovementioned considerations, we have selected a simple and widely used precursor, Iron (II) phthalocyanine (FePc), which was mixed with a conductive high surface area carbon matrix (Ketjenblack EC-600JD). This mixture was subject to pyrolysis at different temperatures (room temperature to 1000 °C) and atmospheres (inert: Ar and slightly reducing: Ar/H_2 95/5 wt%). FePc is considered a model EC used for the ORR and resembles the shape of the heme B contained within the hemoglobin, an important iron-containing oxygen-transport protein that is present in red blood cells. XAS was used to examine the variation of iron speciation during the pyrolysis processes at different temperatures and atmospheres (in-situ). Importantly, a similar set of samples was examined ex-situ using XAS, for comparison. Several other microscopic and spectroscopic tools were also used to analyze the samples (ex-situ). Notably, all the produced samples were investigated electrochemically performing the ORR utilizing a rotating ring disk electrode (RRDE). The variation of Fe coordination and its evolution during pyrolysis identify the iron active site speciation

distribution at different temperatures and atmospheres, allowing the construction of structure-reactivity correlations. This work and methodology provide a novel pathway to design superior-performing ECs by identifying and selecting formulation strategies that facilitate optimal active site configurations. As such, the in-situ characterization, in conjunction with ex-situ surface microscopic and spectroscopic analysis and electrocatalytic measurements is paramount to developing the next-generation ORR ECs for sustainable energy production. We are confident that this modus operandi can be easily translated into other electrochemical reactions and other types of single-atom or nanoparticle-derived electrocatalysts.

2. Experimental

2.1. Samples fabrication

The experimental design was comprised of two different sets of samples; the first set was pyrolyzed in the inert atmosphere of pure argon (Ar) while the second was pyrolyzed in a slightly reducing atmosphere of 95 wt% argon balanced with 5 wt% hydrogen (Ar/H$_2$). The fabrication route first involved a thorough mixing of commercially available carbon black (Ketjenblack EC-600JD, KJB) and iron phthalocyanine (FePc) in a definite proportion of 90 wt% and 10 wt%, correspondingly. The precursors were homogenously mixed by subjecting them to a high-energy ball-milling (EMAX, Retsch Gmbh, Germany) for 1 h at 400 rpm. The homogenized mixture (named as No HT) was then poured into an alumina boat and transferred to a quartz tube, using an atmosphere controlled flange system installed in a horizontal tube furnace (Carbolite). The samples were subsequently pyrolyzed at a desired target temperature (200, 300, 400, 500, 600, 700, 800, 900 and 1000 °C) for 1 h where the heating and cooling ramp rates were maintained at 300 °C h^{-1} in a controlled atmosphere of either Ar or Ar/H$_2$. Before starting the pyrolysis, the quartz tube was purged with the respective gas for at least 30 min to ensure the removal of air from the pyrolyzing system. The produced samples were labeled with respect to their pyrolysis conditions as 'Fe(Atmosphere)_Temperature'. For instance; the sample pyrolyzed at 200 under flowing Ar was given the name 'Fe(Ar)_200' while its counterpart pyrolyzed in an Ar/H$_2$ environment was called 'Fe(Ar/H$_2$)_200'.

2.2. Electrochemical analysis

ORR activities of the fabricated samples were analyzed through the RRDE arrangement (Pine WaveVortex RDE system assembled with a Pine bipotentiostat) as described in previous reports [48,49]. The three-electrode system was set up by connecting a graphite rod, saturated calomel electrode (SCE) and RRDE (E6R2 series) as a counter electrode, reference electrode and working electrode, respectively, where the working electrode was developed by depositing EC ink with 0.6 mg cm^{-2} mass loading on the glassy carbon disk (with an area of 0.2376 cm^2) of RRDE. To prepare the EC ink, 4.5 mg of EC was dispersed in the solvent containing 985 μL isopropanol (Alfa Aesar) and 15 μL of Nafion® D-520 (5 wt%, Alfa Aesar) and the suspension was sonicated for 10 min using probe sonicator followed by agitation in an ultrasonic bath for the next 30 min at room temperature [50,51]. ORR activities were examined in both acidic and alkaline conditions while using oxygen-saturated 0.5 M H$_2$SO$_4$ and 0.1 M KOH, separately, as working electrolyte. The study presents all the potential values referenced according to a reversible hydrogen electrode (RHE) using Eq. 1 as follows:

$$E_{RHE} = E_{SCE} + 0.0591 \times pH + E_{SCE}^{\circ} \tag{1}$$

E_{SCE} is the measured working potential versus SCE whereas E_{SCE}° is the standard potential of SCE reference (0.241 V). Linear sweep voltammograms (LSVs) at the scan rate of 5 mV s^{-1} were obtained by maintaining the potential window between − 0.1–1.2 V vs RHE while fixing

the ring potential of RRDE at 1.2 V vs RHE. Prior to acquiring actual LSVs, the EC was conditioned by applying multiple cyclic voltammetries until a stable behavior was obtained. Finally, peroxide produced (%) and the number of electrons transferred (n) during ORR were calculated by observing the disk current (I$_{disk}$) and ring current (I$_{disk}$) as given in Eq. 2 and Eq. 3, respectively [52].

$$Peroxide \quad (\%) = \frac{200 \times \frac{I_{ring}}{N}}{I_{disk} + \frac{I_{ring}}{N}} \tag{2}$$

$$n = \frac{4I_{disk}}{I_{disk} + \frac{I_{ring}}{N}} \tag{3}$$

2.3. Advanced characterizations

X-ray diffraction (XRD, Rigaku Miniflex 600) was employed to reveal the crystallographic features of the samples in the 2 θ range of 10–80º whereas the structural integrity of the carbonaceous frameworks was studied through Raman spectroscopical measurements (LabRam, Jobin Yvon, France). He-Ne laser (λ = 632.8 nm) was used to illuminate the samples via microscope (BX40, Olympus, Japan) with an objective lens of 50X (numerical aperture of 0.60) while a silicon CCD (Sincerity, Jobin Yvon, France) was used for the signal collection at 200 K.

To carry out CHNS elemental examination, Elementar Vario Microcube Device was used in which the combustion tube and oxidation tube were operating at 1100 °C and 850 °C, respectively.

HRTEM images were acquired using a Thermofisher Talos F200X G2 at an accelerating voltage of 200 kV using a high-speed CETA camera operating at a camera resolution of 4096 × 4096 pixels without any objective aperture. The High-Angle Annular Dark Field images were acquired with a Panther annular STEM detector using a convergent beam with an angle of 10.5 mrad and a camera length of 330 mm. The EDX maps were taken with a Super X spectrometer equipped with four 30 mm^2 silicon drift detectors with a collection angle of 0.7 srad. Data processing and arrangement have been performed with the Thermofisher proprietary software VELOX.

XAS analyses have been performed at the beamline BM-08 LISA of the European Synchrotron Radiation Facility (Grenoble) [53]. A fixed exit double crystal monochromator cooled at Liquid Nitrogen and equipped with Si (111) crystals was used for monochromating the beam whereas a pair of Si mirrors were used for beam collimation and focusing. The beam on the sample site was about 100 × 100 μm. Data were collected in transmission mode using N$_2$-filled ion chambers (IC), a reference foil was inserted after the second IC and its spectrum, read by a third IC was used as an energy reference. For the thermal treatment, the sample was inserted in a microtomo cell [54]. Data were collected at the Iron K-edge (E = 7112 eV) to study its oxidation state, folding, and evolution during the pyrolysis process. For this reason, four sets of measurements have been performed. The samples have been analyzed in two atmospheres: Ar and Ar\H$_2$, for each atmosphere in-situ and ex-situ measurements have been performed. In-situ spectra have been collected directly with the microtome cell, each 100 °C from room temperature (RT) to 800 °C and at 850 °C, with a continuous scan of 120 s. This upper temperature was limited by the heating element used within the microtome cell. Ex-situ spectra have been collected in atmospheric conditions (e.g. exposed directly to air), after heating and cooling the sample in the desired atmosphere, in this case, the samples have been heated in steps of 100 °C in the range RT-1000 as described in the sample fabrication section. XANES and EXAFS spectra have been analyzed using the Athena software (Demeter Package) [55].

X-ray photoelectron spectroscopy (XPS) was conducted on a Kratos AXIS Supra spectrometer with a monochromatic Al Kα source. The high-resolution spectra were obtained using a pass energy of 20 eV at a 0.1 eV step size. CasaXPS software was used to analyze the XPS data. All spectra were calibrated with respect to the sp^2 carbon at 284.5 eV. A Linear

background was employed for the C 1 s and N 1 s spectra, while a Shirley background was used for the Fe 2p spectra. The C 1 s spectra were fit using an 80% Gaussian / 20% Lorentizan function and all other spectra were fit with a 70% Gaussian / 30% Lorentzian function.

3. Results and discussion

3.1. Research design

Herein a methodical investigation has been produced to evaluate the role of the pyrolysis conditions (specifically temperature and atmosphere) on the formation, evolution and transformation of active sites and their ultimate correlations with electrochemical performance. Since the study primarily aimed to analyze the evolutionary pathway of Fe-based moieties during pyrolysis, fine structures of the iron edge through XAS were acquired in both in-situ (spectra acquisition during pyrolysis) and ex-situ (spectra recorded on the samples already pyrolyzed in a tube furnace and exposed to the environment) settings. XAS is an element-sensitive technique and provides a unique set of information about the electronic structure, geometrical arrangements or local symmetries, bonding characteristics and coordination with neighboring atoms of the particular element having a minute concentration in a complex environment. Fine structures mainly consist of two regions (i) X-ray absorption near-edge structure (XANES) and (ii) extended X-ray absorption fine structure (EXAFS) can be obtained in a synchronized way owing to the fast and real-time data acquisition capacity of XAS (will be detailed discussed in the following sections). However, to support the findings of the XAS measurements, complementary ex-situ characterization techniques were employed and the evolution of the Fe-N$_x$-C EC during pyrolysis was deeply analyzed and correlated with the performance aptitudes of the ECs produced at different temperatures and atmospheres. Therefore, the investigational scheme was comprised of two different types of samples: (i) Fe-N$_x$-Cs pyrolyzed in a completely inert atmosphere of pure Ar (indicated by Fe(Ar)) and (ii) Fe-N$_x$-Cs pyrolyzed in a slightly reducing atmosphere of 95 wt% Ar balanced with 5 wt% H$_2$ (Ar/H$_2$) (indicated by Fe(Ar/H$_2$)). For the ex-situ samples fabrication, samples were collected by subjecting the initial mixture to a higher temperature (in the steps of 100 °C) from 200 °C to 1000 °C. The fabrication routes and experimental design are comprehensively discussed in the materials and method section.

3.2. Large-scale characterization

The bulk properties of the samples pyrolyzed in the ex-situ setting were first analyzed soon after their fabrication. Therefore, X-ray diffraction (XRD) patterns of both types of samples were obtained in the 2θ range of 10–80° and presented in Fig. S1 (a & b). From the XRD patterns of the samples pyrolyzed in the slightly reducing atmosphere (Ar/H$_2$), two categorically broader peaks at 2θ position of ca. 25° and 44° were indexed as (002) and (101) planes of carbon (labeled as '♣'), respectively indicating defective and amorphous C [56,57]. At first glance the absence of diffraction peaks corresponding to Fe-based species may nullify the likelihood of their large-scale coalescence and nanoclustering even at the highest pyrolysis temperature of 1000 °C, apparently suggesting the atomic scale homogenous distribution of Fe in the carbonaceous matrix [57–59] (see Fig. S1 (a)). Quite interestingly an unalike drift was experienced in the crystallographic development of the samples pyrolyzed in the pure Ar where the structural integrity of the atomically dispersed Fe in defective carbon seemed to be sustained till 600 °C. However, the samples Fe(Ar)_800 and Fe(Ar)_1000 exhibited a few tiny peaks (labeled as '◆') corresponding to iron oxide (Fe$_3$O$_4$ consistent with the JCPDS# 00–003–0863) which suggests the coalescence and growth of Fe-based nanoparticles in an oxide form at the higher temperatures. Yang et al. have also reported the restriction of metallic nanoclusters formation till 600 °C during the pyrolysis of single atom EC while temperature increments up to 800 °C can give rise to the

formation of nanoclusters [60]. Similarly, through in-situ XRD measurements, Huang et al. also experienced the possible formation of iron carbide at higher temperatures (above 849 °C) [31]. Moreover, in our previous work, we also noticed no oxide nanoparticle formation at 600 °C whereas an evidenced development of the metallic nanoparticles was observed for the samples pyrolyzed at 900 °C [61]. To further explore the carbon-based structure of the achieved ECs, Raman spectra were acquired and presented in Fig. S1 (c). Though this technique does not, generally, give interesting information related to the Fe-containing active sites, the acquired spectra can be useful to characterize the carbonaceous surroundings giving insightful information. The spectra were comprised of characteristic 'D' and 'G' bands, located in the vicinity of ca. 1330 cm^{-1} and 1590 cm^{-1}, respectively. Clearly higher D peaks in each EC specifies the greater density of the structural defects in the carbon matrix. This observation is also consistent with the XRD outcomes showing the dominance of defective and amorphous phase of carbon. The intensity ratio of the D to G band (I$_D$/I$_G$) can be used as an indicator for the estimation of defect density and degree of graphitization. For all the ECs, I$_D$/I$_G$ came out to be higher than unity i.e. typically in the range of 1.41–1.51, which further endorses the higher degree of graphitic imperfections and disorders in carbon. It is worth noting that Ar pyrolyzed samples demonstrated relatively higher I$_D$/I$_G$ (refer to Fig. S1 (c)).

sp^2-type pristine carbon is nearly inactive towards the surface adsorption of O$_2$ and its subsequent electrochemical reduction. Such electro-neutrality of carbon can be interrupted by the doping of nitrogen whose higher electronegativity helps in the chemisorption of O$_2$ on the carbon and hence assist in enhancing the rate of ORR [62,63]. The incorporation of nitrogen into the carbonaceous framework of Fe-N$_x$-Cs is known for efficacious ORR performance in all the pH ranges i.e. acidic, neutral and alkaline [23,37,48,64–66] where each pH of the electrolytic media can give rise to a particular class of FCs. FePc being a co-source of nitrogen and iron was used to functionalize the carbon during pyrolysis. CHNS elemental analysis was carried out to quantify the proportion of nitrogen present in the bulk EC obtained at a given pyrolysis temperature and the achieved outcomes of this analysis are charted in Table S1. The trends of nitrogen doping for both series of ECs i.e. samples pyrolyzed in Ar and the samples pyrolyzed in Ar/H$_2$ are illustrated in Fig. S1 (d). It is noteworthy that as the pyrolysis temperature goes up the corresponding percentage of the doped nitrogen declines, where a drastic slump can be seen after 600 °C in both cases. The inset of Fig. S1 (d) further endorses this fact as the carbon-to-nitrogen ratio initially remains steady however, as the pyrolysis temperature crosses the threshold of 600 °C the ratio increases exponentially which may modify the ORR kinetics and route followed during the activity.

3.3. Surface chemistry

As mentioned before, nitrogen doping can induce different types of active moieties which may perform differently under varying electrolytic conditions. Therefore, the nature and fraction of different nitrogen-based moieties were examined while benefiting from the surface sensitivity of XPS. Importantly, as often the transition metal (TM) used is in low percentage (below 1 wt%), the nitrogen spectrum is used to identify "indirectly" the TM-N$_x$ moieties, additionally, the XPS is sensitive to just a few nanometers of the surface, therefore, wrapping of iron species within the carbon superficial layers may reduce the Fe signals [67,68]. The high-resolution N 1 s spectral signatures of the samples pyrolyzed at different temperatures (from 200 to 1000 °C) under flowing Ar/H$_2$ are provided in Fig. S2, whereas the N 1 s spectra correspond to the second types of samples (pure Ar pyrolysis) are separately presented in the Fig. S3. As a reference, the XPS was also conducted on the non-pyrolyzed mixture (referred to as 'No HT'). N 1 s signatures evolved primarily with five different types of moieties i.e. pyridinic, Fe-N$_x$, pyrrolic, graphitic and NO$_x$, emerging at their typical binding energies (B.E) [23,65, 68–72]. Table S2 and Table S3 demonstrate the distribution of nitrogen

and carbon-based species estimated by XPS examination of Ar/H$_2$ and Ar pyrolyzed samples, respectively. The overall trends in the surface chemistry can be divided into three main regions with respect to pyrolysis temperature where major changes take place: (1) room temperature to 400 °C, (2) 400–800 °C and (3) above 800 °C as categorically displayed in Fig. 1. From Fig. 1(a), the relative evolution of Fe-N$_x$ can be appreciated. It is important to note that the series of the samples pyrolyzed in Ar/H$_2$ showed a positive relationship between the relative proportion of Fe-N$_x$ and pyrolysis temperature, however, in Ar pyrolyzed series initially Fe-N$_x$ increased with temperature and reached its maximum level at 500 °C (sample Fe(Ar)_500) and then started declining where the lowest Fe-N$_x$ was present in the Fe(Ar)_800 and Fe (Ar)_900. This observation is relatable to the XRD outcomes of the Ar pyrolyzed samples where Fe(Ar)_800 and Fe(Ar)_1000 indicated the presence of iron-oxide-based nanoparticles. From the distribution of pyridinic nitrogen displayed in Fig. 1(b), its content initially shot up with temperature to 400 °C for both series of samples. However, in the case of a reducing atmosphere, pyridinic nitrogen moieties came out to be a maximum in the Fe(Ar/H$_2$)_500 and then started diminishing as the pyrolysis temperature increased but after 800 °C more pronounced reduction was witnessed. While for the Ar pyrolyzed counterparts, the highest fraction of pyridinic was obtained at 800 °C and then plummeted drastically. On the other hand, the least amount of pyrrolic nitrogen was witnessed in the range of 500–700 °C for both categories of the ECs and afterward, it began to increase rapidly with temperature as can be seen in Fig. 1(c). From Fig. 1(d), an opposing trend in the distribution of graphitic nitrogen can be seen between Ar and Ar/H$_2$ samples but in any case, the extent of graphitic nitrogen leaned upward after 800 °C which is favorable due to the higher temperatures. Lastly, the NO$_x$ (Fig. 1(e)) demonstrated negative drifts concerning the pyrolysis temperature however, their proportion again increases at the higher temperatures of 900–1000 °C. Fig. 1(f) displays the alteration in the extent of sp^2-type surface carbon at different pyrolysis temperatures where a clear gain in sp^2 content can be seen in the ECs pyrolyzed above 800 °C.

3.4. Morphological investigation

Next, the morphological progressions along with chemical transformations in the pyrolyzed samples were visualized by means of high-resolution transmission electron microscopy (HRTEM). HRTEM images showed that both for pyrolysis in Ar/H$_2$ and Ar the formation of Fe nanoparticles starts between 500 and 600 °C (Fig. S4 & S5). Below this threshold, only amorphous carbon and ruptured graphitic domains exist without the presence of metallic nanoparticles. This fact can be further confirmed by the micrographs reported in Fig. 2, where a comparison of the high-magnification morphology of the as-developed samples is reported. At 400 °C only the carbon framework with a typical mixture of defective graphitic and amorphous domains is present, confirming the atomic level dispersion of Fe-N$_x$ species (Fig. 2(a & b)). On the other hand, at 600 °C in Ar/H$_2$ the formation of nanoparticles consisting of iron and oxygen can be easily seen. Remarkably, these nanoparticles had a core-shell structure with an oxygen-depleted core and an oxygen-rich shell. The HRTEM analysis clearly indicates a core-shell structure with different crystalline features that may be ascribed to a magnetite core with a Fe$_2$O$_3$ shell. Differently, the nanoparticles that emerged in the Ar pyrolyzed samples i.e. Fe(Ar)_600 and Fe(Ar)_800 demonstrated a more condensed structure without any shells (Fig. 2(d & f)). To further explore the elemental distribution in the pyrolyzed samples, a scanning transmission electron microscope (STEM) coupled with energy dispersive X-ray (EDX) was performed, in order to acquire compositional maps, enabling the better visualization of elemental distribution. The acquired high-angle annular dark-field (HAADF) images along with the corresponding EDX area maps for the samples pyrolyzed at 400 °C, 600 °C and 800 °C under flowing Ar/H$_2$ and pure Ar are presented in Fig. 3. At 400 °C, the metallic coalescence and nanoparticle development seemed to be restricted in both pyrolyzing environments. Both Fe(Ar/H$_2$)_400 and Fe(Ar)_400 showed the homogenous distribution of iron and
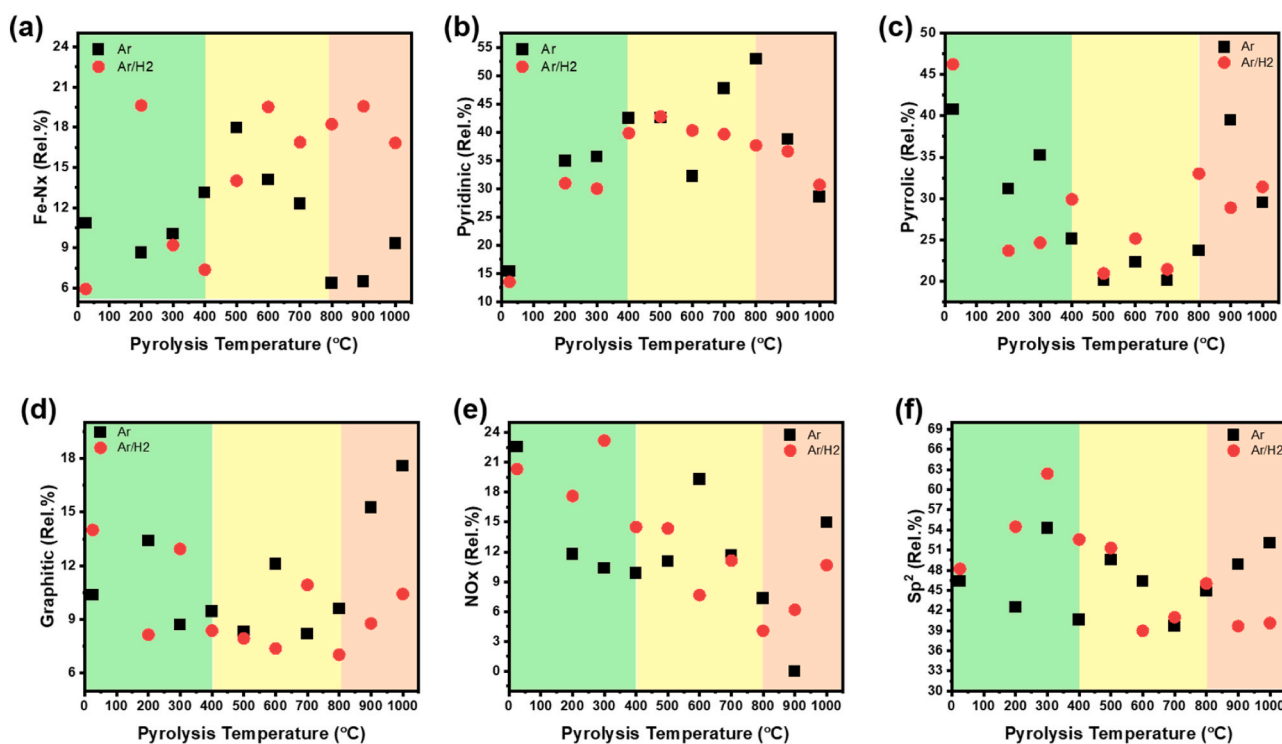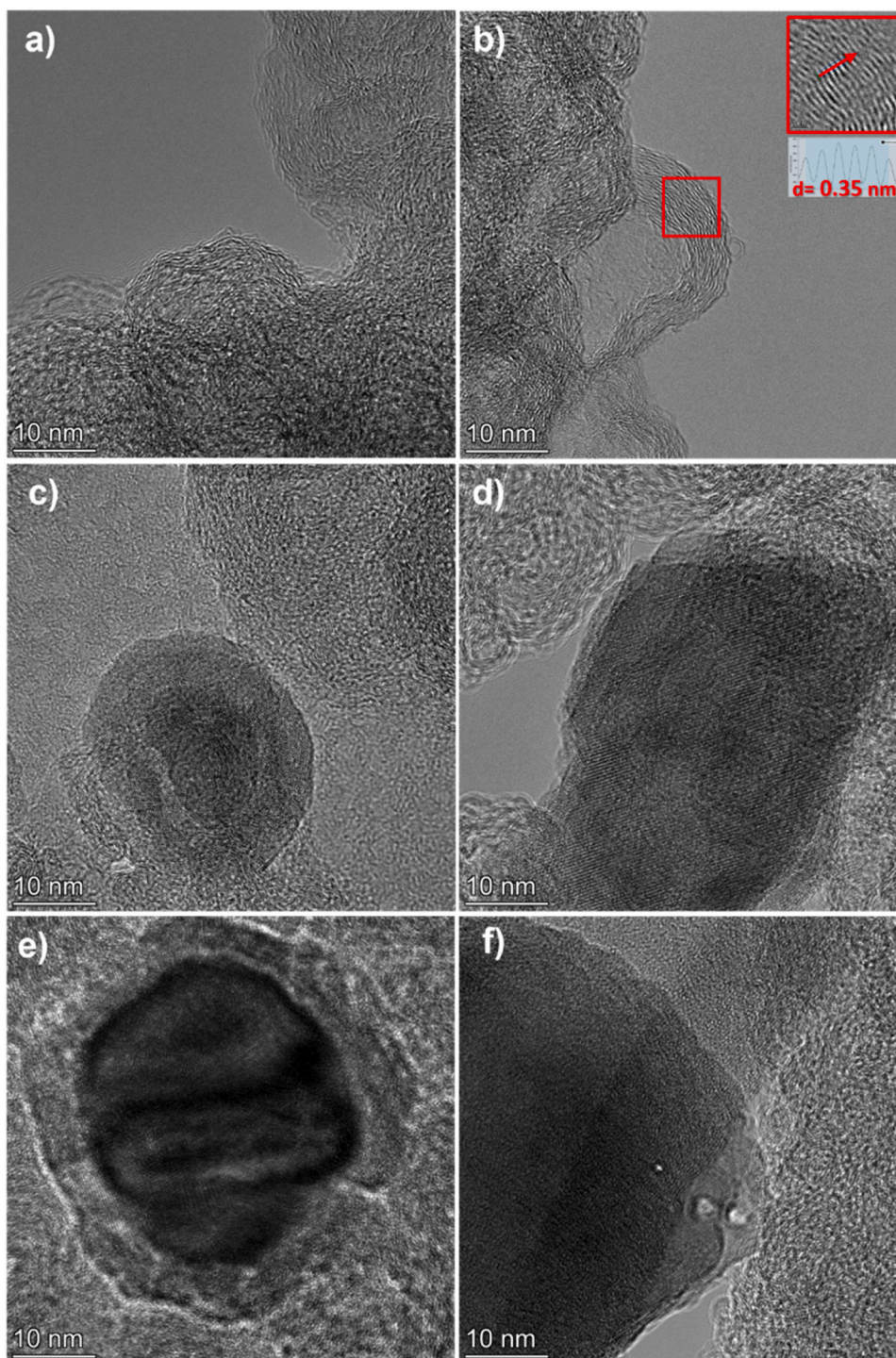

Fig. 1. A relationship between the pyrolysis temperature and the emergence of the nitrogen-based active moieties detected by the XPS. Relative distribution of Fe-N$_x$ (a), pyridinic (b), pyrrolic (c), graphitic (d), NO$_x$ species (e) and sp^2 carbon (f) in the ECs produced at different temperatures under flowing Ar or slightly reducing environment of Ar/H$_2$.

Fig. 2. HRTEM images of the Ar and Ar/H$_2$ pyrolyzed samples. HRTEM micrographs of Fe(Ar/H$_2$)_400 (a), Fe(Ar)_400 (b), Fe(Ar/H$_2$)_600 (c), Fe(Ar)_600 (d), Fe(Ar/H$_2$)_800 (e) and Fe(Ar)_800 (f).

nitrogen throughout the carbon framework. However, cube-like nanoparticles are evident in the samples pyrolyzed at 600 °C and 800 °C. Interestingly, as the temperature increases also the size of nanoparticles increases. It is pertinent to note that in general, the nanoparticles evolved in pure Ar pyrolyzed samples have a larger size compared to those developed in the Ar/H$_2$ counterpart. This might also explain why the peaks of the iron oxide in the XRD patterns are evident in the Ar-only sample (Fig. S1 (b) on XRD). The downward trend in Fe-N$_x$ for Ar pyrolyzed samples after 500 °C also suggests the enhanced diffusion of atomic iron and accelerated coalescence and growth of nanoparticles.

3.5. X-ray absorption spectroscopy

XAS spectra for the speciation of Fe-based moieties during the development of Fe-N$_x$-C under Ar or Ar/H$_2$ were recorded in both in-situ and ex-situ settings. XANES and EXAFS spectra have been analyzed using the Athena software (Demeter Package) [55,73]. The XANES spectra are shown in Fig. 4, and the main features of FePc (1−5) are highlighted on the top axes. In Fig. 4, XANES profiles of the FePc, on the upper plots, the spectra collected on samples pyrolyzed in Ar/H$_2$ atmosphere (Fig. 4(a & b)), on the lower plot, the spectra collected on
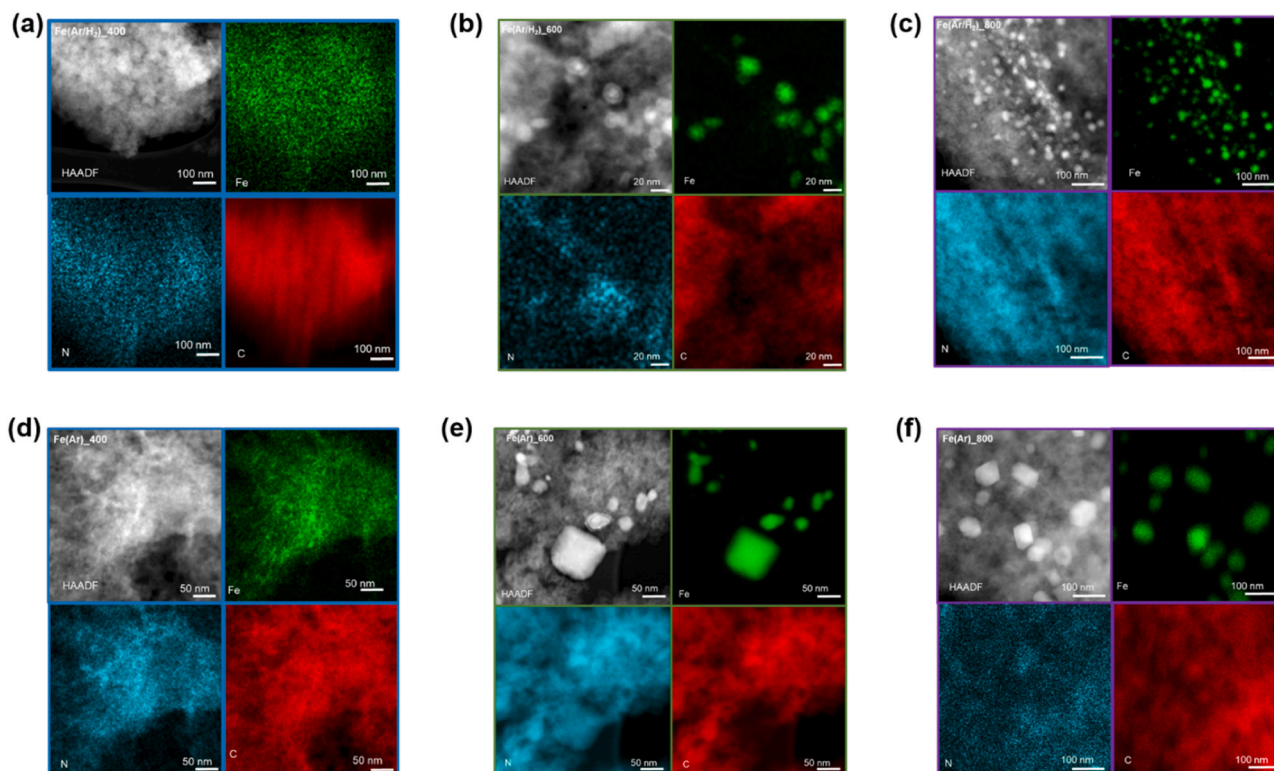
Fig. 3. HAADF-STEM and EDX mapping of the samples pyrolyzed under slightly reducing atmosphere (a) Fe(Ar/H$_2$)_400, (b) Fe(Ar/H$_2$)_600 and (c) Fe(Ar/H$_2$)_800. Whereas corresponding HAADF-STEM and EDX mapping of Ar pyrolyzed samples are shown in (d) Fe(Ar)_400, (e) Fe(Ar)_600 and (f) Fe(Ar)_800.

samples pyrolyzed in Ar atmosphere (Fig. 4(c & d)). On the left, the data collected ex-situ, on the right, the data collected in-situ. In the insets, the region of the pre-peaks is highlighted. The first thing that can be observed, independently from the environment and the analysis condition (in-situ or ex-situ) is that the spectra undergo a significant change between 600 °C and 700 °C. Below these temperatures the spectrum well-resemble the one of FePc, and only rearrangements in the molecular structure take place; above, different phases start to form. To observe the changes in the molecular structure below 600 °C, the pre-peak evolution was studied, as it describes the changes in the co-ordination, folding and symmetry of the central iron; after the formation of the different phases, instead, a linear combination fitting (LCF) of the XANES spectra and the analysis of the EXAFS allows to distinguish the new different phases.

The in-situ and ex-situ measurements show very different behaviors for the spectra below 600 °C, indeed in the case of the ex-situ measurements, few changes occur in this temperature range both in the pre-edge peak region (peaks 1, 2) and above the edge (peaks 3–5). As shown by [74–77], peaks 3–4 are related to *1 s→4pz* transitions while peak 5 is related to *1 s→4px,y* transition, even if in the ex-situ measurements their intensity is stable, in the in-situ experiments, it can be observed that their intensity changes, in particular peak 4 decreases, and the spectrum collected at 600 °C mostly resembles the spectrum of microcrystalline FePc [76]. Instead in the pre-edge region, not only the pre-peaks 1 and 2 are observed, but also a third pre-peak (A), which is less intense in the in-situ spectra collected above 200 °C.

To evaluate the effects of temperature on the symmetry change, a pre-peak fitting has been performed using Python (version 3.10) lmfit (version 1.1.0) package [78,79]. The baseline has been fit with an atan function, while the peaks have been fit with five pseudo-Voigt functions. The fit has been performed in two steps: (I) a pre-fit of the background and (II) a fit of the peaks with a background correction. The intensity of each peak (calculated as the area underneath the peak) has then been reported in Fig. 5).

As can be observed in the ex-situ measurements, not many changes are visible, but a slight decrease of peak A and an increase of peak 2 are detected as the temperature of pyrolysis increases. Instead, for the in-situ measurements, it can observed that pre-peak A decreases and dis-appears in the samples heated at 500 °C, while peak 2 increases signif-icantly. Pre-peaks 1 and A are related to the dipole-forbidden quadruple-allowed 1 s→3d transition, while pre-peak 2 is related to the 1 s→4pz transition. A change of intensity in these two pre-peaks is related to the change of geometry in the system, from C$_{4v}$ (tetragonal pyramidal) to D$_{4 h}$ (tetragonal) symmetry (and vice versa), most probably related to the desorption (adsorption) of oxygen. As stated in [75,76], the increase of temperature in the in-situ measurements shows the desorption of oxygen and the change from a pyramidal to a planar geometry. In par-allel, the small changes in the pre-peaks of the ex-situ measurements suggest that after being exposed to air, oxygen is again adsorbed by the FePc with the formation of (FePc)$_2$O. TM-N$_x$-Cs are already known for their biomimetic behavior similar to natural enzymes i.e. heme-copper oxidase (cytochrome-c-oxidase and ubiquinol oxidase) or hemoglobin [20]. TM-N$_x$-Cs precisely complement the architectural and functional fidelities of such enzymes where the central metallic atom i.e. Fe has a strong affinity for the binding of oxygen. In the hemoglobin, the heme Fe (II) is coordinated with four porphyrins (nitrogen-containing rings) li-gands and when it interacts with oxygen, it instantaneously binds to it, producing the octahedral Fe-complex. A similar scenario prevails during the ex-situ measurements as the FePc-derived Fe-N$_x$-C ECs are exposed to the room atmosphere after pyrolysis and the oxygen from the sur-rounding tends to attach on the Fe sites as a fifth ligand which was not observed during the in-situ measurements due to the controlled envi-ronment and oxygen desorption due to temperature and absence of oxygen in the surrounding atmosphere. This observed phenomenon is interestingly fully in line with an established methodology to estimate active-site density and turnover frequency of TM-N$_x$-Cs using CO cryo adsorption in which EC is cleaned before CO sorption via thermal annealing at 600 °C [80,81] because O$_2$ is supposed to bind to Fe-N$_x$ as
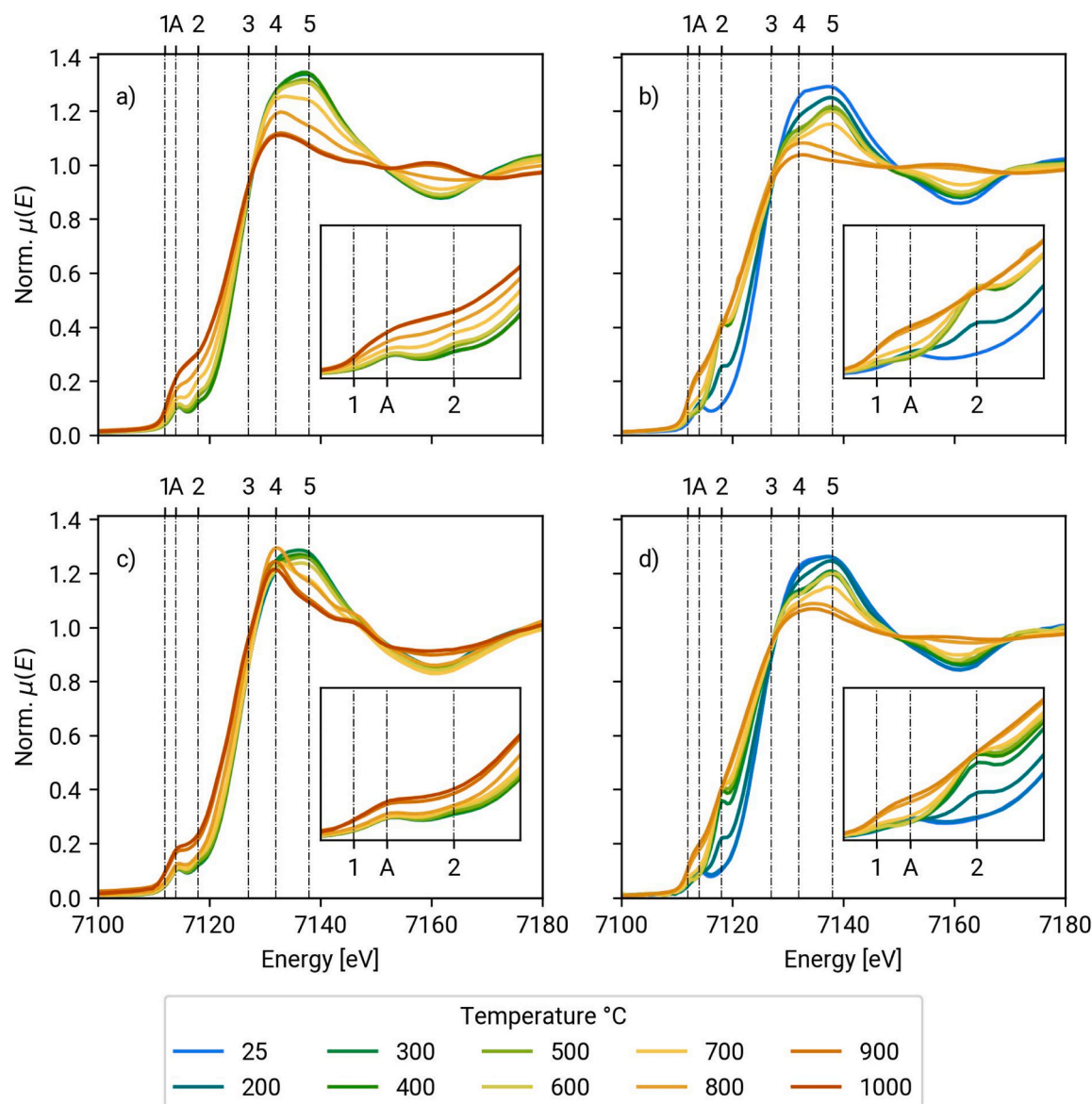
Fig. 4. XANES profiles of the FePc: a) spectra collected ex-situ in Ar/H$_2$ atmosphere, b) spectra collected in-situ in Ar/H$_2$ atmosphere, c) spectra collected ex-situ in Ar atmosphere, d) spectra collected in-situ in Ar atmosphere.

the EC exposes to open environment [81,82].

The changes above 600 °C reflect the formation of new phases which can be better described by observing the EXAFS spectra (Fig. S6 in the SI) and their Fourier transform (Fig. 6). At lower temperatures, the main peaks observed are those at 1.5 Å due to the backscattering from the four N atoms, at 2.6 Å (backscattering from the eight pyrrole carbon atoms bonded to nitrogen) and at 3.2 Å (related to the backscattering from the four bridge nitrogen atoms). The left tail of the 1.5 Å peak may cover the peak related to the Fe-O backscattering which is found at 1.2 Å.

In the ex-situ measurements, the changes are nearly negligible until 700 °C. In the in-situ measurements, a decrease is observed in the peaks' intensity; besides, it must be considered that the lattice vibration caused by the increase in temperature increases the thermal disorder, which smears out the EXAFS oscillation. The main changes are observed above 700 °C: in the ex-situ Ar/H$_2$ samples, an intense peak at 2.1 Å and two peaks at 4.1 Å and 4.8 Å appear, related to Fe-Fe bond in an FCC geometry (Austenite or γ-Fe, Fig. S7 in the SI); in the sample pyrolyzed in Ar atmosphere, the iron peaks are not present, but a wider band around 2.5–3 Å, where lies Fe-Fe and Fe-O peaks of magnetite, can be observed. This observation truly agrees with the XRD and HRTEM outcomes where

the samples pyrolyzed above 600 °C in the Ar atmosphere categorically showed the growth of oxide nanoparticles.

The transformations occurring during the pyrolysis can be investigated with the XANES LCF. As reference spectra, the spectra of magnetite was employed, already found with XRD analyses, α-Fe, γ-Fe and FePc. The Pc reference employed for the in-situ measurements is the one collected at 500 °C, as the oxygen desorption has to be considered, while for the ex-situ measurements, the sample heated at 200 °C was considered. The results of the LCF (see Figs. S8–9) are summarized in Fig. 7. It is possible to clearly observe the decrease in the Pc percentage and the formation of new phases during the pyrolysis. In the ex-situ measurements, the presence of magnetite is higher, especially in those pyrolyzed in Ar atmosphere and magnetite seems to be the principal phase. In general, the BCC structure of iron (α-Fe) is more present in the samples measured in-situ. However, considering that for those measurements, the data were collected up to 850 °C, an overall increase of metallic iron during the pyrolysis can be observed. Hence, it can be inferred that at higher temperatures, particularly above 600 °C, the ECs tend to break the single-atom configuration due to considerable coalescence-assisted growth of metallic nanoparticles and this
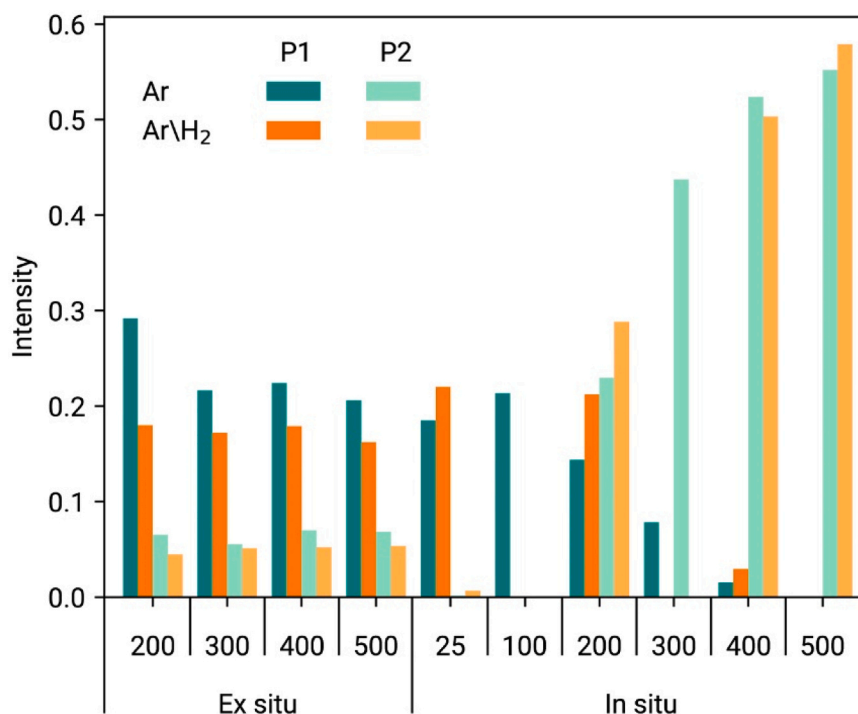
Fig. 5. Pre-peak intensities for the spectra collected below 600 °C in both ex-situ and in-situ measurements. In orange, the data for the samples pyrolyzed in Ar/H$_2$ atmosphere are represented and in green are those for the spectra pyrolyzed in the Ar atmosphere.

phenomenon might alter the electrocatalytic activity of the ORR.

3.6. ORR activity in acidic media

In the subsequent phase of the study, RRDE was used to probe the electrocatalytic activity parameters. ORR activities of the developed ECs under different pyrolysis circumstances were studied in acidic and alkaline media to simulate their ultimate cathodic employment in proton-exchange membrane fuel cells (PEMFCs) and anion-exchange membrane fuel cells (AEMFCs), respectively. The RRDE outcomes in acidic media (O$_2$-saturated 0.5 M H$_2$SO$_4$) are illustrated in Fig. 8 and Fig. S10 (EC loading of 0.6 mg cm^{-2}). From the linear sweep voltammograms (LSVs) presented in panel (a) of Fig. 8, ORR kinetics launched by the ECs can be appreciated. In the beginning, as the pyrolysis temperature increased under both Ar and Ar/H$_2$ flow, separately, the LSVs of the corresponding evolved ECs tended to shift towards the right side where the most positive shifts were observed for Fe(Ar)_600 and Fe(Ar/H$_2$)_600, indicating a relative decrease in the overpotentials. However, ORR activities started declining for the ECs obtained above 600 °C as the corresponding onset potentials (E$_{onset}$) and limiting current densities (J$_{limiting}$) went on diminishing as a function of pyrolysis temperature. The worst ORR kinetics were exhibited by the samples obtained above 900 °C (refer to Fig. S10(a)). The trends of E$_{onset}$ and E$_{1/2}$ in the acidic medium are additionally provided in Fig. S11(a), signifying an initial upshift in the E$_{onset}$ and E$_{1/2}$ up to 600 °C followed by a drastic drop for ECs acquired at and above 700 °C. Another interesting contrast also prevails between the pyrolysis atmospheres where the samples fabricated under pure Ar demonstrated considerably higher J$_{limiting}$. Such a trend of performance could be linked with the structure and surface chemistry that evolved during the pyrolysis. As the pyrolysis temperature increases the proportion of Fe-N$_x$ and pyridinic nitrogen sites increases and reaches its maxima in the vicinity of 600 °C. Interestingly initially pyrrolic and graphitic nitrogen also followed a negative trend up to 600 °C and then increased as the temperature increased. Overall both types of samples (series pyrolyzed in Ar or Ar/H$_2$) displayed a negative correlation with the pyrolysis temperature as illustrated in

Fig. S11 (b-c). Moreover, to figure out the reduction pathway of the O$_2$, the ring current densities were collected and have been demonstrated in Fig. 8(b) and Fig. S10 (b). The ring current densities increased as overpotential proceeded, however, the trend after 800 °C changed importantly. The ring current densities of Fe(Ar)_800 and Fe(Ar/H$_2$)_800 increased initially and then dropped at the higher overpotential values and such fashion was also observed for the samples fabricated at 900 and 1000 °C (Fig. S10 (b)). The ultimate upshot of the aforesaid divergences can be visualized in the aptitudes of peroxide generation. Fe(Ar)_600 and Fe(Ar/H$_2$)_400 exhibited the least peroxide production throughout the potential window and gave the impression of a direct tetra electronic electro-reduction with electron transformations (n) close to 4 as can be seen in Fig. 8(c-d). However, samples fabricated at and above 800 °C suggested a 2 × 2 e$^-$ reduction route which means that the peroxide produced at the lower overpotential would have reduced stepwise at the secondary sites as the overpotential proceeded. The insets of Fig. S11 (b-c) present the peroxide production capacities where the Ar pyrolyzed ECs exhibited a clear positive relationship between peroxide production and pyrolysis temperature.

3.7. ORR in alkaline media

It is well-known in the community that as the pH of the electrolytic media shifts the reaction, the role of the active moieties also gets modified which ultimately alters the overall reaction mechanism [48, 83–87]. Therefore, the ORR performance of the ECs achieved under varying pyrolysis conditions was additionally monitored in an alkaline medium (O$_2$-saturated 0.1 M KOH) using RRDE in a similar arrangement. From the LSVs provided in Fig. 9(a) and Fig. S12 (a), negative tendencies in the ORR activities can be seen as the pyrolysis temperature proceeds. The E$_{onset}$ and the E$_{1/2}$ calculated in the alkaline media for the corresponding ECs came out to be significantly higher compared to the values estimated under acidic conditions. According to Brocato et al. within the acidic range of pH the rate-determining step is independent of proton concentration whereas in alkaline conditions the first electron transfer constitutes the rate-determining step and in addition, the
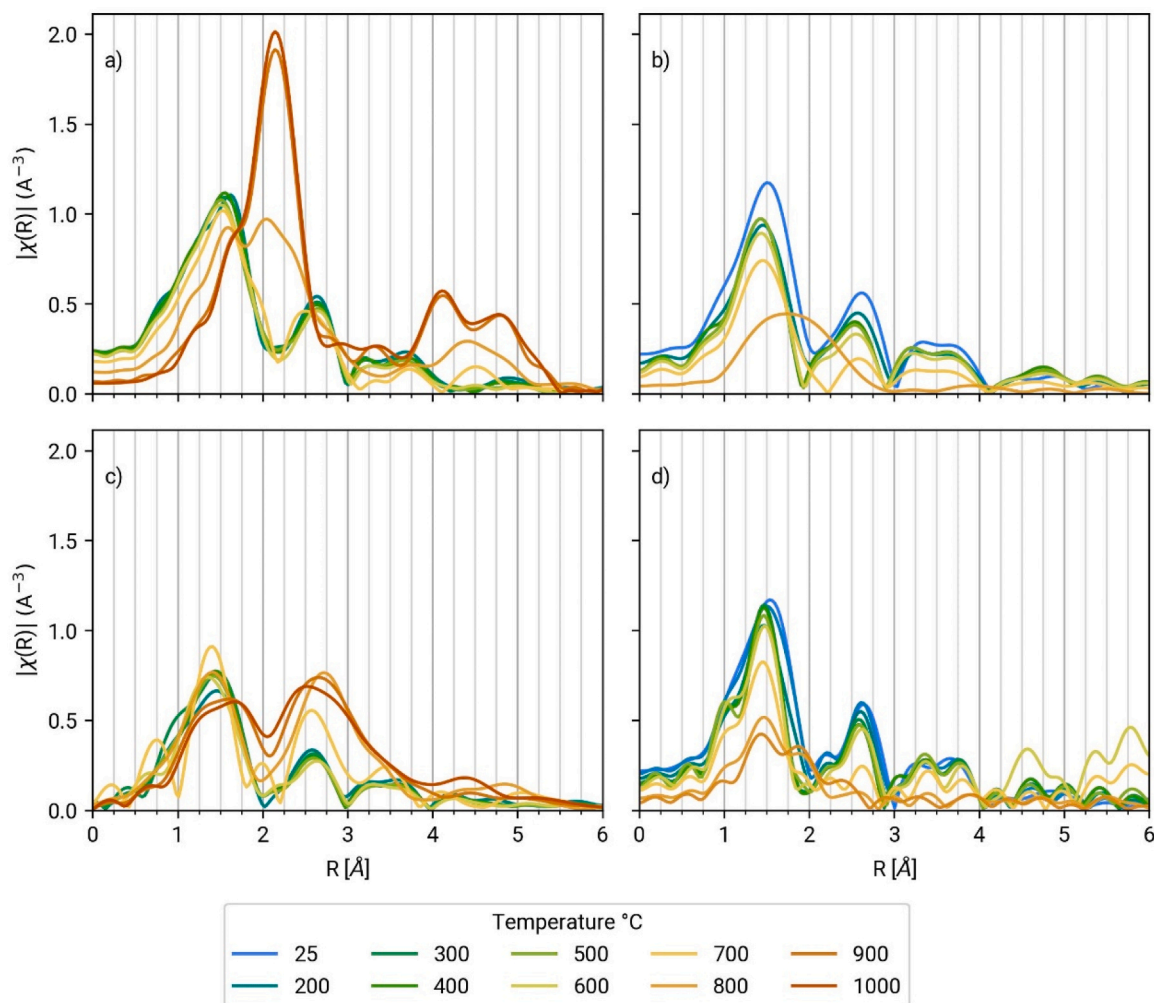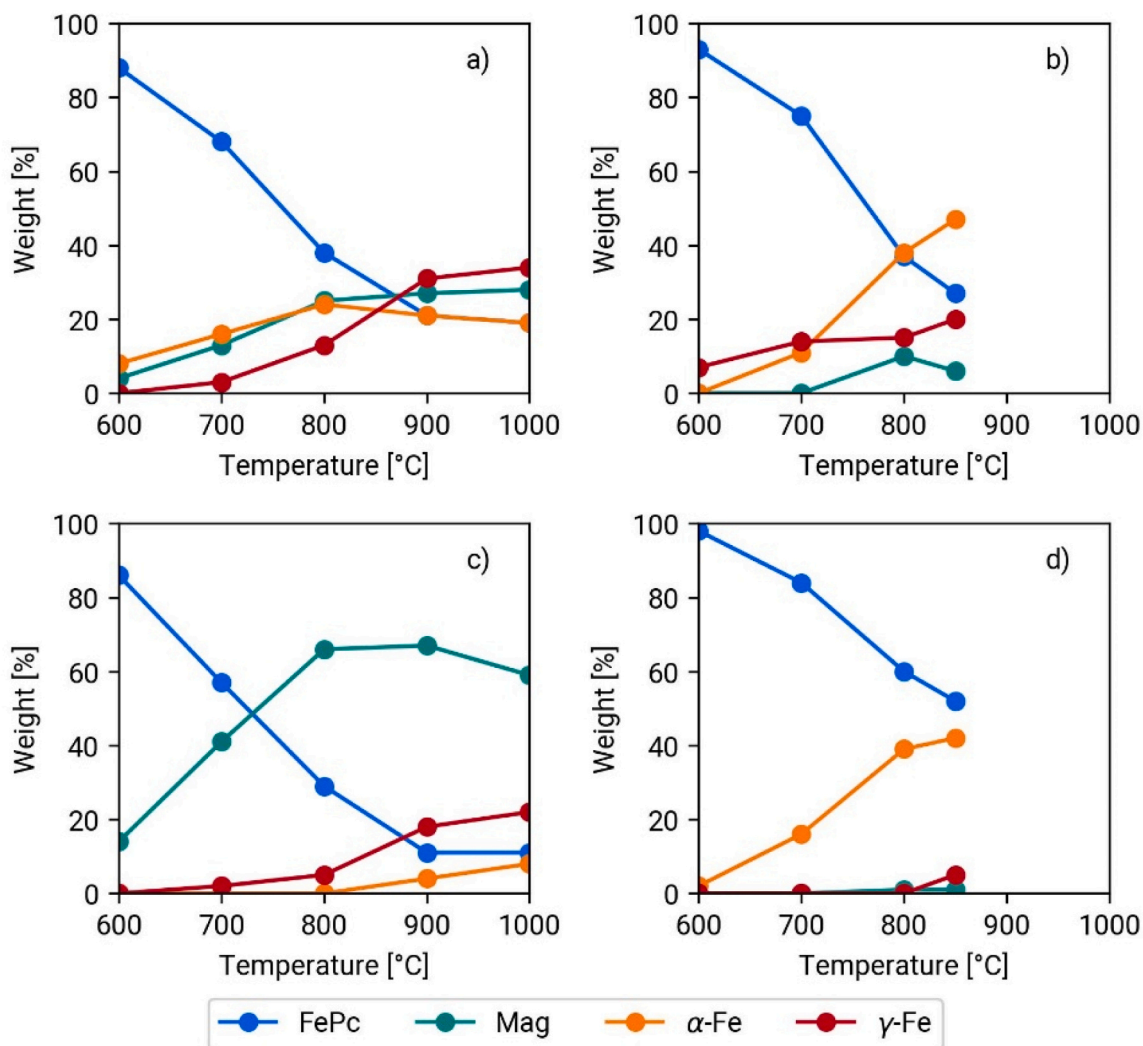
Fig. 6. Fourier Transform of the EXAFS in R-space, uncorrected phase. a) data collected ex-situ in Ar/H$_2$ atmosphere, b) data collected in-situ in Ar/H$_2$ atmosphere, c) data collected ex-situ in Ar atmosphere, d) data collected in-situ in Ar atmosphere.

peroxide intermediate forming in the alkaline medium is relatively stable on the Fe^{2+} sites, opposed to the intermediate forming in acidic medium and hence to some extent augments the half-wave potential [83]. With each increment in the pyrolysis temperature, the estimated values of the E$_{onset}$ and E$_{1/2}$ for the corresponding EC went on declining (Fig. S13 (a)). The optimum E$_{onset}$ and E$_{1/2}$ were realized by the ECs pyrolyzed between 600 and 700 °C in both atmospheres i.e. Ar and Ar/H$_2$, however, a prompt reduction in the E$_{onset}$ and E$_{1/2}$ was seen afterward. Again, the samples pyrolyzed in Ar owing to their higher E$_{1/2}$ and J$_{limiting}$, performed slightly better than the ones pyrolyzed in Ar/H$_2$. Temperature-dependent shrinkage of J$_{limting}$ was more prominent in the alkaline media. In parallel, the ring current densities (Fig. 9(b)) increased as the overpotential continued. Correspondingly, peroxide production also increased with respect to the pyrolysis temperature, where the samples fabricated in pure Ar atmosphere produced relatively less peroxide. It is important to underline that the peroxide yield at higher overpotentials was significantly increased after 600 °C, specifying an absolute alteration in the reduction pathway also in an alkaline medium. Fig. S13 (b-c), categorically illustrates the downward shift in the J$_{limiting}$ with a definite upsurge in the peroxide production along the progression of pyrolysis temperatures in both types of atmospheres.

3.8. Structure-to-property relationships

To affirm the relationship between the evolved structural features and corresponding ORR activities, surface chemistry was first associated with performance descriptors through principal component analysis (PCA) and the achieved biplots are presented in Fig. 10. PCA underlines the correlations and anti-correlation among independent variables in which multi-colinearities exist and through linear (or non-linear) combinations it compresses the data into the most important principal components (PCs). Therefore, PCA has already been opportunely applied to relate the performance to the structural attributes of the ORR ECs derived at different stages of the fabrication pathways [64,70,88, 89]. The first PC demonstrates the maximum variance possible while the second PC (orthogonally aligned) possesses the largest possible variance [90,91]. The variables such as surface active species identified via XPS, performance parameters recorded through RRDE and pyrolysis temperatures that have greater relevancy are clustered as a group on the biplot. From biplots in Fig. 10 (a-b) it can be seen that samples acquired in the range of 500–700 °C both in Ar and Ar/H$_2$ are directly linked with the ORR kinetic parameters i.e. E$_{onset}$, E$_{1/2}$ and J$_{limiting}$ in the acidic medium due to abundance of Fe-N$_x$ and pyridinic nitrogen as they are present in close vicinity of each other on the biplots. Similar correlations were revealed when PCA was applied to Ar and Ar/H$_2$ pyrolyzed samples for the alkaline medium as given in Fig. 10 (c-d). The peak ORR performance for the ECs pyrolyzed in the temperature range of 600 °C in both atmospheres has already been discussed in detail in the previous sections that could be attributed to a suitable combination of the most active moieties as revealed through HRTEM, XPS and XAS. Till 600 °C, an excellent balance of optimal nitrogen amount (that drastically decreases afterward as shown by CHNS analysis), high Fe-N$_x$ content, a

Fig. 7. Linear combination fitting of the pyrolyzed samples. The scatter plot represents the percentage of the different components, in blue the FePc, in green magnetite, orange iron and red austenite. Results for a) data collected ex-situ in Ar/H$_2$ atmosphere, b) data collected in-situ in Ar/H$_2$ atmosphere, c) data collected ex-situ in Ar atmosphere, d) data collected in-situ in Ar atmosphere.

good proportion of pyridinic nitrogen, limited pyrolytic and graphitic nitrogen, defect-rich carbonaceous structure (relatively lower sp^2) and most importantly restriction in the coalescence and growth of Fe-based oxide NPs prevail. However, the whole scenario extraordinarily changes above 600 °C. It is well-known that Fe-N$_x$ are the primary sites to carry out tetra-electronic electro-reduction of oxygen [23,92,93] and a drop in quantity of Fe-N$_x$ at higher temperatures could be one of the major reasons for the decay in the performance. Recently, Lu et al. also experienced the extraordinary performance of their multivalent hybrid EC particularly due to a higher proportion of pyridinic and M-Nx active sites [94]. Pyrrolic nitrogen is known to launch bi-electronic ORR, whereas pyridinic nitrogen can reduce the generated peroxide into water and complete the reaction in the second step [23,95,96]. Typically pyridinic nitrogen and hydrogenated nitrogen functionalities such as pyrrolic are predominately formed at the edges of the graphitic planes by substituting the carbon atoms located at the edge and making the edge defects electrochemically more active than the in-plane carbon atoms [37,96]. The strong electron affinity of nitrogen present in such defects makes the adjacent carbon more electropositive which facilitates the adsorption of oxygen and intermediates during ORR and enhances the reaction rates [37,97]. However, the carbon atoms next to the pyrrolic nitrogen are relatively more electropositive than those present in the surrounding of pyridinic nitrogen [63]. Quite captivatingly, between

500 and 700 °C (in both Ar and Ar/H$_2$) the least amount of pyrrolic nitrogen with higher pyridinic nitrogen and Fe-N$_x$ content can synergistically lead to the direct and complete O$_2$ reduction in a four-electron fashion. Moreover, the graphitic nitrogen could be another factor to limit the ORR activity which was at a maximum in the ECs pyrolyzed above 800 °C and showed the least E$_{onset}$ and E$_{1/2}$ in every situation. Graphitic nitrogen is widely known to contribute to peroxide formation during the ORR [64,93,98] as the positive charge of the graphitic nitrogen imparts a negative charge on the surrounding carbon through a screening effect that hinders the adsorption of oxygen.

To extend the understanding of the origin of the activity of individual relationships between surface chemistry and performance parameters have been provided in supporting information (Fig. S14-17). However, the pyridinic nitrogen seemed to have a marginal impact on the enhancement of E$_{1/2}$ of the Fe(Ar) series but pyridinic nitrogen made a positive relationship with the peroxide production. Moreover, pyrrolic and graphitic nitrogen became the cause of the subsequent reduction in the E$_{1/2}$ where increments in the graphitic nitrogen content not only diminished the J$_{limiting}$ but also led to peroxide enhancement. Interestingly, NO$_x$ made beneficial correlations where E$_{1/2}$ and J$_{limiting}$ clearly increased with an increase in the NO$_x$ proportion, while reducing the extent of peroxide formation Fig. S14 (j-i). On the other hand, in the Fe (Ar/H$_2$) samples, Fe-N$_x$ did not show any direct relationship with the E$_{1/}$
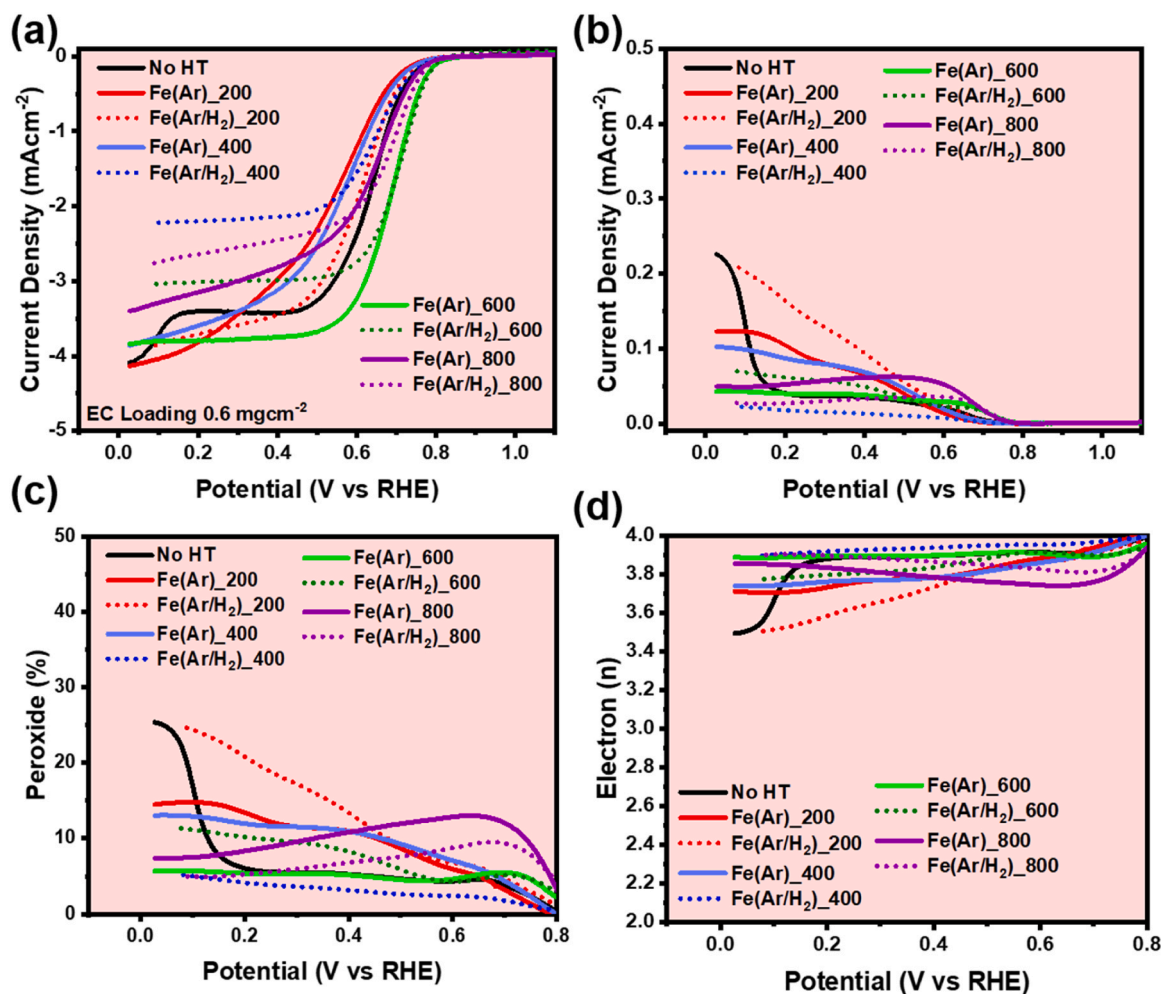
Fig. 8. ORR activity of samples pyrolyzed under different pyrolysis conditions, LSVs in 0.5 M H_2SO_4 at 5 mVs^{-1} (a), ring current densities (b), generation of peroxide (c) and electron transfer trends (f).

$_2$ and $J_{limiting}$, while positively influencing the production of peroxide as can be seen in the first three panels of Fig. S15. Here a bit of care is needed, the performance parameters cannot be solely related to the presence of Fe-N_x in the Fe(A/H_2) samples despite their proportional increases with temperature. In fact, other peroxide-producing moieties are also formed at higher pyrolysis temperatures. Remarkably, pyrrolic nitrogen although slightly reducing the $J_{limiting}$ clearly lowered the peroxide production where the 2×2 ORR pathway may prevail Fig. S15 (h-i). Furthermore, graphitic nitrogen tended to lower the $E_{1/2}$ but didn't show any appreciable relationship with peroxide generation, whereas NO_x similarly increased the $J_{limiting}$. While associating the surface chemistry with the performance descriptors observed during the ORR measurements in the alkaline medium, the Fe(Ar) series demonstrated similar trends observed during the acidic measurements. Fig. S16 (a-c) revealed the positive relationship between $E_{1/2}$ or $J_{limiting}$ and Fe-N_x where it also emerged as the obstructer of peroxide production. Where pyridinic nitrogen opted the way of lowering $J_{limiting}$, pyrrolic nitrogen tended to increase it, while reducing the $E_{1/2}$. Graphitic nitrogen again pushed the ORR activity towards a bi-electronic fashion by diminishing the $E_{1/2}$ and $J_{limiting}$ together with a drastic upsurge in the peroxide production as the trends presented in Fig. S16 (g-i). Moreover, NO_x showed a positive relationship with kinetic parameters and a tendency to lower the peroxides. The trends for the Ar/H_2 pyrolyzed samples in the alkaline (Fig. S17) almost remain the same as they demonstrated in the acidic medium.

The next most important factor controlling the ORR activity is the speciation of Fe-based moieties as revealed through HRTEM and XAS analysis. Through XAS analysis, it was confirmed that till 600 °C Fe is largely present as an atomically dispersed moiety while maintaining the configuration of FePc (Fe-N_4) but certainly also Fe-N_3 and Fe-N_2 active sites are present, however, it is impossible to discriminate these active sites. The ex-situ measurements confirmed that oxygen is present and bound with the central Fe atom forming the fifth ligand. However, Fe-N_x is undoubtedly the most active inherent site of the single atom Fe-N_x-Cs [99,100]. Therefore, enhanced kinetics of the ORR activity with direct tetra-electronic reduction pathway was witnessed till 600 °C and afterward went on decaying. Xie et al. have recently confirmed the superior ORR activity due to atomically dispersed Fe–N_x active sites which show optimum adsorption and then reduction of oxygen [100]. Temperature increments after 600 °C led to the coalescence and growth of iron oxide nanoparticles. Through XRD and XAS, it was established that the nanoparticles formed during pyrolysis under flowing Ar are Fe_3O_4 whereas the relatively smaller nanoparticles evolved in the Ar/H_2 have core-shell-like structures as revealed through HRTEM analysis where the shell seemed to be richer in oxygen. The effects of Fe_3O_4 co-presence in the ECs with active sites of the type Fe-N_x-C towards ORR have also been studied in previous reports [96,101,102]. From the electrochemical outcomes, the least activity was observed for the ECs pyrolyzed at higher temperatures where the peroxide production was also enhanced significantly. However, in acidic media, the 2×2 reduction pathway can be observed, where the peroxide yield was higher initially but at a larger overpotential, it was reduced. Tylus and co-workers have undeniably
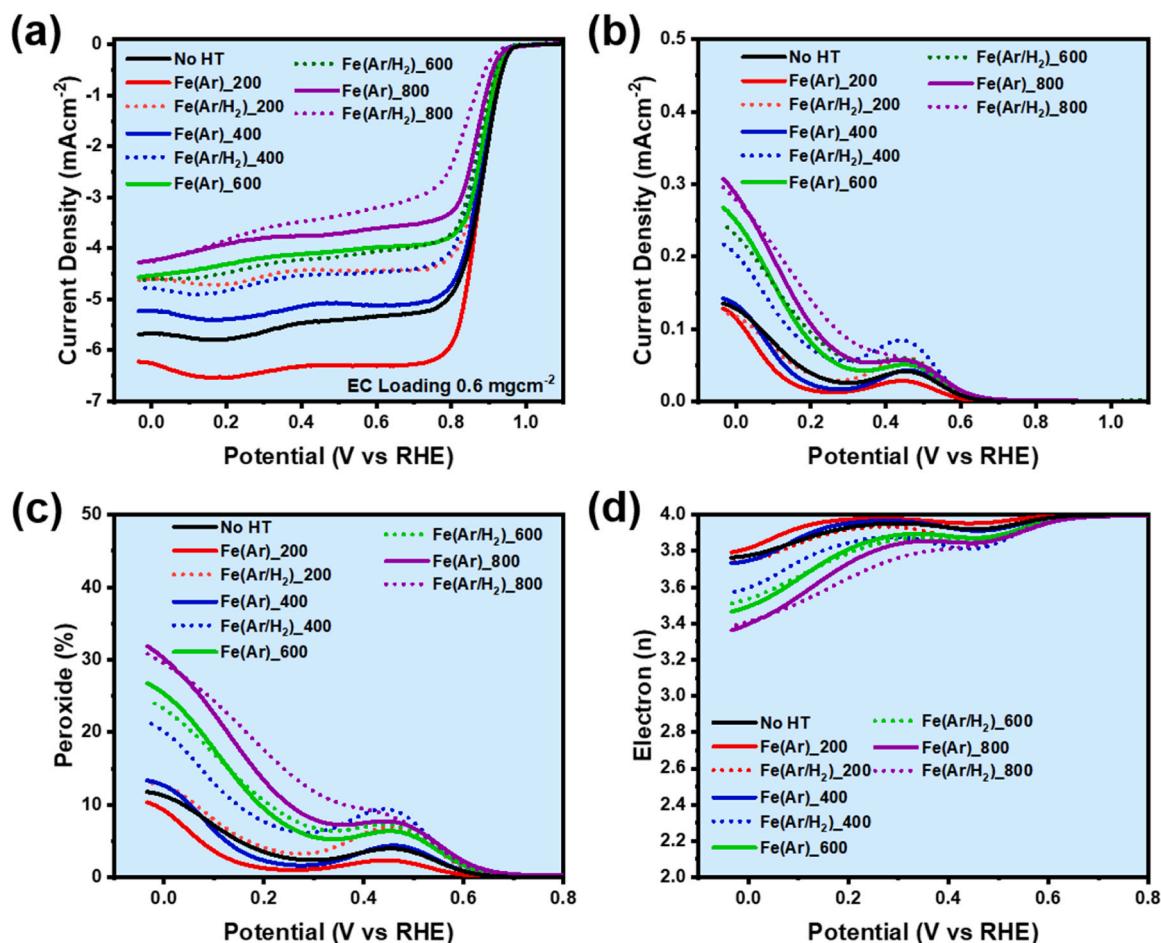
Fig. 9. Alkaline ORR activity of samples pyrolyzed under different pyrolysis conditions, LSVs in 0.1 M KOH at 5 mVs^{-1} (a), ring current densities (b), generation of peroxide (c) and electron transfer trends (f).

elucidated that in alkaline media Fe-N$_x$ are the prime sites for ORR, however, in acidic conditions, Fe-based nanoparticles in close vicinity of Fe-N$_x$ act as a secondary site to the stepwise reduction of the produced peroxide to water [66]. Nevertheless, a lower proportion of Fe-N$_x$ and the evolution of nanoparticles in the ECs pyrolyzed at higher temperatures affect the ORR activity and pathway.

4. Conclusions

In a nutshell, a systematic approach was adopted to study the temperature- and atmosphere-dependent developments of active site structures in the Fe-N$_x$-C. Commercial electroconductive carbon black (Ketjenblack EC-600JD) was functionalized with 10 wt% FePc during the course of pyrolysis from room temperature to 1000 °C in two different atmospheres i.e. inert atmosphere by pure Ar and slightly reducing atmosphere of Ar/H$_2$. Through a combination of advanced microscopic and spectroscopic techniques the evolution, growth and transformation of active moieties were elucidated and a structure-property relationship was constructed by testing the ORR response of the samples acquired at different temperatures and under different atmospheres using RRDE in acidic and alkaline media. The best performing in terms of the highest E$_{onset}$ and direct tetra electronic reduction pathway was observed with the Fe(Ar)_600 and Fe(Ar/H$_2$)_600, in both media. Above this temperature not only the overpotentials were significantly increased but also the reduction pathway was modified into a 2 × 2 fashion. Through XRD, HRTEM and XAS, it was observed that till 600 °C an atomic level distribution of Fe in Fe-N$_x$ coordination is maintained and afterward oxide nanoparticles start

emerging, where the growth of the nanoparticles was accelerated in the Ar atmosphere. XRD and XAS confirmed the presence of Fe$_3$O$_4$ type nanoparticles in the samples pyrolyzed above 600 °C under pure Ar, while with the help of HRTEM a core-shell-like structure of Fe oxide nanoparticles was visualized in Ar/H$_2$ pyrolyzed samples where the shell was richer in oxygen content. Remarkably, XAS fine structures for in-situ and ex-situ measurements showed interesting results indicating a substantial structural modification due to the attachment of the oxygen as a fifth ligand (pyramidal structure) as the ex-situ samples were exposed to air after the pyrolysis. In-depth surface chemistry evaluation through XPS also confirmed the best balance of nitrogen-based moieties in the vicinity of 600 °C with the highest proportion of Fe-N$_x$ and pyridinic structures, lower content of pyrrolic and reduced content of graphitic nitrogen. However, the individual response of the pyrolysis atmosphere varies slightly. By developing a processing-structure-performance relationship, it is confirmed that pyrolysis at 600 °C is the optimum temperature to have the best ORR electrocatalytic activity due to a favorable combination of surface chemistry, suitable morphological features and atomic level dispersion of Fe-N$_x$ active sites with restriction of nanoparticle coalescence and growth. While the pyrolysis under flowing Ar produces a slightly improved outcome.

CRediT authorship contribution statement

Mohsin Muhyuddin: Conceptualization, Data curation, Formal Analysis, Investigation. **Enrico Berretti**: Conceptualization, Data curation, Formal Analysis, Investigation. **Seyed Ariana Mirshokraee**: Data curation, Formal Analysis, Investigation. **Jacopo Orsilli:** Data curation,
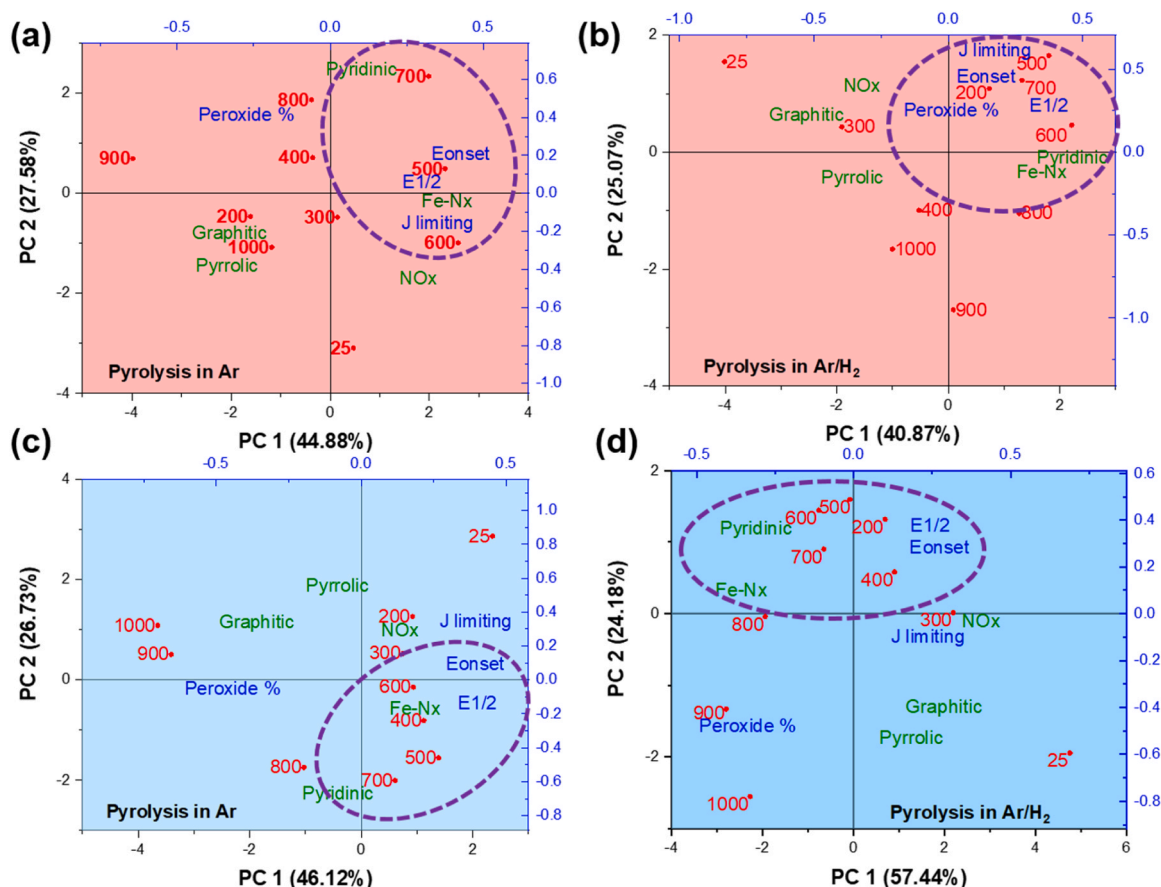
Fig. 10. Biplots acquired through principal component analysis (PCA) making the relationships among the surface active moieties detected by XPS and performance parameters of ECs derived at different temperatures during pyrolysis under Ar or Ar/H$_2$. PCA biplot for the performance dependency on Ar pyrolyzed samples in acidic media (a), Ar/H$_2$ pyrolyzed samples in acidic media (b), Ar pyrolyzed samples in alkaline media (c) and Ar/H$_2$ pyrolyzed samples in alkaline media (d) at different temperatures from 25° to 1000°C.

Declaration of Competing Interest

The authors declare that they have no known competing financial interests or personal relationships that could have appeared to influence the work reported in this paper.

Data Availability

Data will be made available on request.

Acknowledgments

Appendix A. Supporting information

Supplementary data associated with this article can be found in the online version at doi:10.1016/j.apcatb.2023.123515.

References

[1] Z. Abdin, A. Zafaranloo, A. Rafiee, W. Mérida, W. Lipiński, K.R. Khalilpour, Hydrogen as an energy vector, Renew. Sustain. Energy Rev. 120 (2020), 109620, https://doi.org/10.1016/j.rser.2019.109620.

[2] M. Yue, H. Lambert, E. Pahon, R. Roche, S. Jemei, D. Hissel, Hydrogen energy systems: a critical review of technologies, applications, trends and challenges, Renew. Sustain. Energy Rev. 146 (2021), 111180, https://doi.org/10.1016/j.rser.2021.111180.

[3] J.O. Abe, A.P.I. Popoola, E. Ajenifuja, O.M. Popoola, Hydrogen energy, economy and storage: review and recommendation, Int. J. Hydrog. Energy 44 (2019) 15072–15086, https://doi.org/10.1016/j.ijhydene.2019.04.068.

[4] M. Muhyuddin, G. Tseberlidis, M. Acciarri, O. Lori, M. D'Arienzo, M. Cavallini, P. Atanassov, L. Elbaz, A. Lavacchi, C. Santoro, Molybdenum disulfide as hydrogen evolution catalyst: from atomistic to materials structure and electrocatalytic performance, J. Energy Chem. 87 (2023) 256–285, https://doi.org/10.1016/j.jechem.2023.08.011.

[5] Md.M. Hossen, Md.S. Hasan, Md.R.I. Sardar, J. bin Haider, Mottakin, K. Tammeveski, P. Atanassov, State-of-the-art and developmental trends in platinum group metal-free cathode catalyst for anion exchange membrane fuel cell (AEMFC), Appl. Catal. B: Environ. (2022), 121733, https://doi.org/10.1016/j.apcatb.2022.121733.

[6] J. Lindorfer, D.C. Rosenfeld, H. Böhm, 23 - Fuel Cells: Energy Conversion Technology, in: T.M. Letcher (Ed.), Future Energy (Third Edition), Elsevier, 2020, pp. 495–517, https://doi.org/10.1016/B978-0-08-102886-5.00023-2.

[7] A.G. Olabi, T. Wilberforce, M.A. Abdelkareem, Fuel cell application in the automotive industry and future perspective, Energy 214 (2021), 118955, https://doi.org/10.1016/j.energy.2020.118955.

[8] C. Qin, S. Tian, W. Wang, Z.-J. Jiang, Z. Jiang, Advances in platinum-based and platinum-free oxygen reduction reaction catalysts for cathodes in direct methanol fuel cells, Frontiers in Chemistry. 10 (2022). https://www.frontiersin.org/articles/10.3389/fchem.2022.1073566 (accessed December 23, 2022).

[9] Y. Nie, L. Li, Z. Wei, Recent advancements in Pt and Pt-free catalysts for oxygen reduction reaction, Chem. Soc. Rev. 44 (2015) 2168–2201, https://doi.org/10.1039/C4CS00484A.

[10] W. Wang, Q. Jia, S. Mukerjee, S. Chen, Recent insights into the oxygen-reduction electrocatalysis of Fe/N/C materials, ACS Catal. 9 (2019) 10126–10141, https://doi.org/10.1021/acscatal.9b02583.

[11] J. Cui, Q. Chen, X. Li, S. Zhang, Recent advances in non-precious metal electrocatalysts for oxygen reduction in acidic media and PEMFCs: an activity, stability and mechanism study, Green. Chem. 23 (2021) 6898–6925, https://doi.org/10.1039/D1GC01040A.

[12] M. Muhyuddin, P. Mustarelli, C. Santoro, Recent advances in waste plastic transformation into valuable platinum-group metal-free electrocatalysts for oxygen reduction reaction, ChemSusChem 14 (2021) 3785–3800, https://doi.org/10.1002/cssc.202101252.

[13] Y. He, S. Liu, C. Priest, Q. Shi, G. Wu, Atomically dispersed metal–nitrogen–carbon catalysts for fuel cells: advances in catalyst design, electrode performance, and durability improvement, Chem. Soc. Rev. 49 (2020) 3484–3524, https://doi.org/10.1039/C9CS00903E.

[14] L. Yang, J. Shui, L. Du, Y. Shao, J. Liu, L. Dai, Z. Hu, Carbon-based metal-free ORR electrocatalysts for fuel cells: past, present, and future, Adv. Mater. 31 (2019), 1804799, https://doi.org/10.1002/adma.201804799.

[15] M.-X. Chen, L. Tong, H.-W. Liang, Understanding the catalytic sites of metal–nitrogen–carbon oxygen reduction electrocatalysts, Chem. – A Eur. J. 27 (2021) 145–157, https://doi.org/10.1002/chem.202002427.

[16] E. Giordano, E. Berretti, L. Capozzoli, A. Lavacchi, M. Muhyuddin, C. Santoro, I. Gatto, A. Zaffora, M. Santamaria, Boosting DMFC power output by adding sulfuric acid as a supporting electrolyte: effect on cell performance equipped with platinum and platinum group metal-free cathodes, J. Power Sources 563 (2023), 232806, https://doi.org/10.1016/j.jpowsour.2023.232806.

[17] K.-Y. Chen, Y.-X. Huang, R.-C. Jin, B.-C. Huang, Single atom catalysts for use in the selective production of hydrogen peroxide via two-electron oxygen reduction reaction: mechanism, activity, and structure optimization, Appl. Catal. B: Environ. 337 (2023), 122987, https://doi.org/10.1016/j.apcatb.2023.122987.

[18] C. Chen, Z.-J. Tang, J.-Y. Li, C.-Y. Du, T. Ouyang, K. Xiao, Z.-Q. Liu, MnO enabling highly efficient and stable Co-Nx/C for oxygen reduction reaction in both acidic and alkaline media, Adv. Funct. Mater. 33 (2023), 2210143, https://doi.org/10.1002/adfm.202210143.

[19] R. Venegas, F.J. Recio, J. Riquelme, K. Neira, J.F. Marco, I. Ponce, J.H. Zagal, F. Tasca, Biomimetic reduction of O2 in an acid medium on iron phthalocyanines axially coordinated to pyridine anchored on carbon nanotubes, J. Mater. Chem. A. 5 (2017) 12054–12059, https://doi.org/10.1039/C7TA02381B.

[20] K. Singh, F. Razmjooei, J.-S. Yu, Active sites and factors influencing them for efficient oxygen reduction reaction in metal-N coordinated pyrolyzed and non-pyrolyzed catalysts: a review, J. Mater. Chem. A 5 (2017) 20095–20119, https://doi.org/10.1039/C7TA05222G.

[21] J.H. Zagal, M. Specchia, P. Atanassov, Mapping transition metal-MN4 macrocyclic complex catalysts performance for the critical reactivity descriptors, Curr. Opin. Electrochem. 27 (2021) 100683, https://doi.org/10.1016/j.coelec.2020.100683.

[22] C.Z. Loyola, S. Ureta-Zañartu, J.H. Zagal, F. Tasca, Activity volcano plots for the oxygen reduction reaction using FeN4 complexes: From reported experimental data to the electrochemical meaning, Curr. Opin. Electrochem. 32 (2022), 100923, https://doi.org/10.1016/j.coelec.2021.100923.

[23] K. Artyushkova, A. Serov, S. Rojas-Carbonell, P. Atanassov, Chemistry of multitudinous active sites for oxygen reduction reaction in transition metal–nitrogen–carbon electrocatalysts, J. Phys. Chem. C. 119 (2015) 25917–25928, https://doi.org/10.1021/acs.jpcc.5b07653.

[24] Q. Liu, Y. Wang, Z. Hu, Z. Zhang, Iron-based single-atom electrocatalysts: synthetic strategies and applications, RSC Adv. 11 (2021) 3079–3095, https://doi.org/10.1039/D0RA08223F.

[25] T. Asset, P. Atanassov, Iron-nitrogen-carbon catalysts for proton exchange membrane fuel cells, Joule 4 (2020) 33–44, https://doi.org/10.1016/j.joule.2019.12.002.

[26] D. Testa, G. Zuccante, M. Muhyuddin, R. Landone, A. Scommegna, R. Lorenzi, M. Acciarri, E. Petri, F. Soavi, L. Poggini, L. Capozzoli, A. Lavacchi, N. Lamanna, A. Franzetti, L. Zoia, C. Santoro, Giving new life to waste cigarette butts: transformation into platinum group metal-free electrocatalysts for oxygen reduction reaction in acid, neutral and alkaline environment, Catalysts 13 (2023) 635, https://doi.org/10.3390/catal13030635.

[27] F. Lu, K. Fan, L. Cui, B. Li, Y. Yang, L. Zong, L. Wang, Engineering FeN4 active sites onto nitrogen-rich carbon with tubular channels for enhanced oxygen reduction reaction performance, Appl. Catal. B: Environ. 313 (2022), 121464, https://doi.org/10.1016/j.apcatb.2022.121464.

[28] X.-T. Wu, L.-J. Peng, K. Xiao, N. Li, Z.-Q. Liu, Rational design and synthesis of hollow Fe–N/C electrocatalysts for enhanced oxygen reduction reaction, Chem. Commun. 57 (2021) 5258–5261, https://doi.org/10.1039/D1CC00460C.

[29] C. Ouyang, X. Wang, Recent progress in pyrolyzed carbon materials as electrocatalysts for the oxygen reduction reaction, Inorg. Chem. Front. 7 (2019) 28–36, https://doi.org/10.1039/C9QI00962K.

[30] Z. Chen, D. Higgins, A. Yu, L. Zhang, J. Zhang, A review on non-precious metal electrocatalysts for PEM fuel cells, Energy Environ. Sci. 4 (2011) 3167–3192, https://doi.org/10.1039/C0EE00558D.

[31] Y. Huang, Y. Chen, M. Xu, T. Asset, P. Tieu, A. Gili, D. Kulkarni, V. De Andrade, F. De Carlo, H.S. Barnard, A. Doran, D.Y. Parkinson, X. Pan, P. Atanassov, I. V. Zenyuk, Catalysts by pyrolysis: Direct observation of chemical and morphological transformations leading to transition metal-nitrogen-carbon materials, Mater. Today 47 (2021) 53–68, https://doi.org/10.1016/j.mattod.2021.02.006.

[32] Y. Chen, Y. Huang, M. Xu, T. Asset, X. Yan, K. Artyushkova, M. Kodali, E. Murphy, A. Ly, X. Pan, I.V. Zenyuk, P. Atanassov, Catalysts by pyrolysis: Direct observation of transformations during re-pyrolysis of transition metal-nitrogen-carbon materials leading to state-of-the-art platinum group metal-free electrocatalyst, Mater. Today 53 (2022) 58–70, https://doi.org/10.1016/j.mattod.2022.01.016.

[33] J. Li, L. Jiao, E. Wegener, L.L. Richard, E. Liu, A. Zitolo, M.T. Sougrati, S. Mukerjee, Z. Zhao, Y. Huang, F. Yang, S. Zhong, H. Xu, A.J. Kropf, F. Jaouen, D. J. Myers, Q. Jia, Evolution pathway from iron compounds to Fe1(II)–N4 sites through gas-phase iron during pyrolysis, J. Am. Chem. Soc. 142 (2020) 1417–1423, https://doi.org/10.1021/jacs.9b11197.

[34] N. Cui, K. Bi, W. Sun, Q. Wu, Y. Li, T. Xu, B. Lv, S. Zhang, Effect of pyrolysis conditions on the performance of Co–doped MOF–derived carbon catalysts for oxygen reduction reaction, Catalysts 11 (2021) 1163, https://doi.org/10.3390/catal11101163.

[35] P.G. Santori, F.D. Speck, J. Li, A. Zitolo, Q. Jia, S. Mukerjee, S. Cherevko, F. Jaouen, Effect of pyrolysis atmosphere and electrolyte pH on the oxygen reduction activity, stability and spectroscopic signature of FeNx moieties in Fe-N-C catalysts, J. Electrochem. Soc. 166 (2019) F3311, https://doi.org/10.1149/2.0371907jes.

[36] A. Zitolo, V. Goellner, V. Armel, M.-T. Sougrati, T. Mineva, L. Stievano, E. Fonda, F. Jaouen, Identification of catalytic sites for oxygen reduction in iron- and nitrogen-doped graphene materials, Nat. Mater. 14 (2015) 937–942, https://doi.org/10.1038/nmat4367.

[37] S. Kabir, K. Artyushkova, A. Serov, P. Atanassov, Role of nitrogen moieties in N-doped 3D-graphene nanosheets for oxygen electroreduction in acidic and alkaline media, ACS Appl. Mater. Interfaces 10 (2018) 11623–11632, https://doi.org/10.1021/acsami.7b18651.

[38] F. Vallejos-Burgos, S. Utsumi, Y. Hattori, X. García, A.L. Gordon, H. Kanoh, K. Kaneko, L.R. Radovic, Pyrolyzed phthalocyanines as surrogate carbon catalysts: Initial insights into oxygen-transfer mechanisms, Fuel 99 (2012) 106–117, https://doi.org/10.1016/j.fuel.2012.03.055.

[39] M.A.C. de Oliveira, V.C.A. Ficca, R. Gokhale, C. Santoro, B. Mecheri, A. D'Epifanio, S. Licoccia, P. Atanassov, Iron(II) phthalocyanine (FePc) over carbon support for oxygen reduction reaction electrocatalysts operating in alkaline electrolyte, J. Solid State Electrochem 25 (2021) 93–104, https://doi.org/10.1007/s10008-020-04537-x.

[40] R. Jasinski, A new fuel cell cathode catalyst, Nature 201 (1964) 1212–1213, https://doi.org/10.1038/2011212a0.

[41] S. Yang, Y. Yu, X. Gao, Z. Zhang, F. Wang, Recent advances in electrocatalysis with phthalocyanines, Chem. Soc. Rev. 50 (2021) 12985–13011, https://doi.org/10.1039/D0CS01605E.

[42] M. Musilov, J. Mrha, J. Jindra, Carbon electrodes with phthalocyanine catalyst in acid medium, J. Appl. Electrochem. 3 (1973) 213–218, https://doi.org/10.1007/BF00619163.

[43] V.S. Bagotzky, M.R. Tarasevich, K.A. Radyushkina, O.A. Levina, S.I. Andrusyova, Electrocatalysis of the oxygen reduction process on metal chelates in acid electrolyte, J. Power Sources 2 (1978) 233–240, https://doi.org/10.1016/0378-7753(78)85014-9.

[44] J.A.R. van Veen, H.A. Colijn, J.F. van Baar, On the effect of a heat treatment on the structure of carbon-supported metalloporphyrins and phthalocyanines, Electrochim. Acta 33 (1988) 801–804, https://doi.org/10.1016/S0013-4686(98)80010-8.

[45] Á. García, T. Haynes, M. Retuerto, P. Ferrer, L. Pascual, M.A. Peña, M. Abdel Salam, M. Mokhtar, D. Gianolio, S. Rojas, Effect of the thermal treatment of Fe/N/C catalysts for the oxygen reduction reaction synthesized by pyrolysis of covalent organic frameworks, Ind. Eng. Chem. Res. 60 (2021) 18759–18769, https://doi.org/10.1021/acs.iecr.1c02841.

[46] U.I. Kramm, J. Herranz, N. Larouche, T.M. Arruda, M. Lefèvre, F. Jaouen, P. Bogdanoff, S. Fiechter, I. Abs-Wurmbach, S. Mukerjee, J.-P. Dodelet, Structure of the catalytic sites in Fe/N/C-catalysts for O2 -reduction in PEM fuel cells, Phys. Chem. Chem. Phys. 14 (2012) 11673–11688, https://doi.org/10.1039/C2CP41957B.

[47] J. Li, M.T. Sougrati, A. Zitolo, J.M. Ablett, I.C. Oğuz, T. Mineva, I. Matanovic, P. Atanassov, Y. Huang, I. Zenyuk, A. Di Cicco, K. Kumar, L. Dubau, F. Maillard, G. Dražić, F. Jaouen, Identification of durable and non-durable FeNx sites in Fe–N–C materials for proton exchange membrane fuel cells, Nat. Catal. 4 (2021) 10–19, https://doi.org/10.1038/s41929-020-00545-2.

[48] M. Muhyuddin, D. Testa, R. Lorenzi, G.M. Vanacore, F. Poli, F. Soavi, S. Specchia, W. Giurlani, M. Innocenti, L. Rosi, C. Santoro, Iron-based electrocatalysts derived from scrap tires for oxygen reduction reaction: evolution of synthesis-structure-performance relationship in acidic, neutral and alkaline media, Electrochim. Acta 433 (2022), 141254, https://doi.org/10.1016/j.electacta.2022.141254.

[49] S. Zago, M. Bartoli, M. Muhyuddin, G.M. Vanacore, P. Jagdale, A. Tagliaferro, C. Santoro, S. Specchia, Engineered biochar derived from pyrolyzed waste tea as a carbon support for Fe-N-C electrocatalysts for the oxygen reduction reaction, Electrochim. Acta 412 (2022), 140128, https://doi.org/10.1016/j.electacta.2022.140128.

[50] M. Muhyuddin, J. Filippi, L. Zoia, S. Bonizzoni, R. Lorenzi, E. Berretti, L. Capozzoli, M. Bellini, C. Ferrara, A. Lavacchi, C. Santoro, Waste face surgical mask transformation into crude oil and nanostructured electrocatalysts for fuel cells and electrolyzers, ChemSusChem 15 (2022), e202102351, https://doi.org/10.1002/cssc.202102351.

[51] M. Muhyuddin, N. Zocche, R. Lorenzi, C. Ferrara, F. Poli, F. Soavi, C. Santoro, Valorization of the inedible pistachio shells into nanoscale transition metal and nitrogen codoped carbon-based electrocatalysts for hydrogen evolution reaction and oxygen reduction reaction, Mater. Renew. Sustain Energy 11 (2022) 131–141, https://doi.org/10.1007/s40243-022-00212-5.

[52] S.A. Mirshokraee, M. Muhyuddin, R. Morina, L. Poggini, E. Berretti, M. Bellini, A. Lavacchi, C. Ferrara, C. Santoro, Upcycling of waste lithium-cobalt-oxide from spent batteries into electrocatalysts for hydrogen evolution reaction and oxygen reduction reaction: a strategy to turn the trash into treasure, J. Power Sources 557 (2023), 232571, https://doi.org/10.1016/j.jpowsour.2022.232571.

[53] A. Puri, G.O. Lepore, F. d'Acapito, The New Beamline LISA at ESRF: performances and perspectives for earth and environmental sciences, Condens. Matter 4 (2019) 12, https://doi.org/10.3390/condmat4010012.

[54] D. Bellet, B. Gorges, A. Dallery, P. Bernard, E. Pereiro, J. Baruchel, A 1300 K furnace for in situ X-ray microtomography, J. Appl. Cryst. 36 (2003) 366–367, https://doi.org/10.1107/S0021889803001158.

[55] B. Ravel, M. Newville, ATHENA, ARTEMIS, HEPHAESTUS: data analysis for X-ray absorption spectroscopy using IFEFFIT, J. Synchrotron Rad. 12 (2005) 537–541, https://doi.org/10.1107/S0909049505012719.

[56] C. Zhu, Q. Shi, B.Z. Xu, S. Fu, G. Wan, C. Yang, S. Yao, J. Song, H. Zhou, D. Du, S. P. Beckman, D. Su, Y. Lin, Hierarchically porous M–N–C (M = Co and Fe) single-atom electrocatalysts with robust MNx active moieties enable enhanced ORR performance, Adv. Energy Mater. 8 (2018), 1801956, https://doi.org/10.1002/aenm.201801956.

[57] M. Muhyuddin, A. Friedman, F. Poli, E. Petri, H. Honig, F. Basile, A. Fasolini, R. Lorenzi, E. Berretti, M. Bellini, A. Lavacchi, L. Elbaz, C. Santoro, F. Soavi, Lignin-derived bimetallic platinum group metal-free oxygen reduction reaction electrocatalysts for acid and alkaline fuel cells, J. Power Sources 556 (2023), 232416, https://doi.org/10.1016/j.jpowsour.2022.232416.

[58] C. Xin, W. Shang, J. Hu, C. Zhu, J. Guo, J. Zhang, H. Dong, W. Liu, Y. Shi, Integration of morphology and electronic structure modulation on atomic iron-nitrogen-carbon catalysts for highly efficient oxygen reduction, Adv. Funct. Mater. 32 (2022), 2108345, https://doi.org/10.1002/adfm.202108345.

[59] X. Luo, X. Wei, H. Wang, W. Gu, T. Kaneko, Y. Yoshida, X. Zhao, C. Zhu, Secondary-atom-doping enables robust Fe–N–C single-atom catalysts with enhanced oxygen reduction reaction, Nano-Micro Lett. 12 (2020), 163, https://doi.org/10.1007/s40820-020-00502-5.

[60] H. Yang, L. Shang, Q. Zhang, R. Shi, G. Waterhouse, L. Gu, T. Zhang, A universal ligand mediated method for large scale synthesis of transition metal single atom catalysts, Nat. Commun. 10 (2019) 1–9, https://doi.org/10.1038/s41467-019-12510-0.

[61] S.A. Mirshokraee, M. Muhyuddin, R. Lorenzi, G. Tseberlidis, C.L. Vecchio, V. Baglio, E. Berretti, A. Lavacchi, C. Santoro, Litchi-derived platinum group metal-free electrocatalysts for oxygen reduction reaction and hydrogen evolution reaction in alkaline media, SusMat 3 (2023) 248–262, https://doi.org/10.1002/sus2.121.

[62] L. Yang, J. Shui, L. Du, Y. Shao, J. Liu, L. Dai, Z. Hu, Carbon-based metal-free ORR electrocatalysts for fuel cells: past, present, and future, Adv. Mater. 31 (2019), 1804799, https://doi.org/10.1002/adma.201804799.

[63] K. Gong, F. Du, Z. Xia, M. Durstock, L. Dai, Nitrogen-doped carbon nanotube arrays with high electrocatalytic activity for oxygen reduction, Science 323 (2009) 760–764, https://doi.org/10.1126/science.1168049.

[64] C. Santoro, A. Serov, R. Gokhale, S. Rojas-Carbonell, L. Stariha, J. Gordon, K. Artyushkova, P. Atanassov, A family of Fe-N-C oxygen reduction electrocatalysts for microbial fuel cell (MFC) application: Relationships between

[65] surface chemistry and performances, Appl. Catal. B: Environ. 205 (2017) 24–33, https://doi.org/10.1016/j.apcatb.2016.12.013.

[65] A. Serov, K. Artyushkova, P. Atanassov, Fe-N-C oxygen reduction fuel cell catalyst derived from carbendazim: synthesis, structure, and reactivity, Adv. Energy Mater. 4 (2014), 1301735, https://doi.org/10.1002/aenm.201301735.

[66] U. Tylus, Q. Jia, K. Strickland, N. Ramaswamy, A. Serov, P. Atanassov, S. Mukerjee, Elucidating oxygen reduction active sites in pyrolyzed metal–nitrogen coordinated non-precious-metal electrocatalyst systems, J. Phys. Chem. C. 118 (2014) 8999–9008, https://doi.org/10.1021/jp500781v.

[67] L. Peng, J. Yang, Y. Yang, F. Qian, Q. Wang, D. Sun-Waterhouse, L. Shang, T. Zhang, G.I.N. Waterhouse, Mesopore-Rich Fe–N–C catalyst with FeN4–O–NC single-atom sites delivers remarkable oxygen reduction reaction performance in alkaline media, Adv. Mater. 34 (2022), 2202544, https://doi.org/10.1002/adma.202202544.

[68] K. Artyushkova, Misconceptions in interpretation of nitrogen chemistry from x-ray photoelectron spectra, J. Vac. Sci. Technol. A 38 (2020), 031002, https://doi.org/10.1116/1.5135923.

[69] M. Kodali, C. Santoro, A. Serov, S. Kabir, K. Artyushkova, I. Matanovic, P. Atanassov, Air breathing cathodes for microbial fuel cell using Mn-, Fe-, Co- and Ni-containing platinum group metal-free catalysts, Electrochim. Acta 231 (2017) 115–124, https://doi.org/10.1016/j.electacta.2017.02.033.

[70] C. Santoro, S. Rojas-Carbonell, R. Awais, R. Gokhale, M. Kodali, A. Serov, K. Artyushkova, P. Atanassov, Influence of platinum group metal-free catalyst synthesis on microbial fuel cell performance, J. Power Sources 375 (2018) 11–20, https://doi.org/10.1016/j.jpowsour.2017.11.039.

[71] K. Artyushkova, B. Kiefer, B. Halevi, A. Knop-Gericke, R. Schlogl, P. Atanassov, Density functional theory calculations of XPS binding energy shift for nitrogen-containing graphene-like structures, Chem. Commun. 49 (2013) 2539–2541, https://doi.org/10.1039/C3CC40324F.

[72] K. Wan, G.-F. Long, M.-Y. Liu, L. Du, Z.-X. Liang, P. Tsiakaras, Nitrogen-doped ordered mesoporous carbon: synthesis and active sites for electrocatalysis of oxygen reduction reaction, Appl. Catal. B: Environ. 165 (2015) 566–571, https://doi.org/10.1016/j.apcatb.2014.10.054.

[73] S.A. Mirshokraee, M. Muhyuddin, J. Orsilli, E. Berretti, L. Capozzoli, A. Lavacchi, C.L. Vecchio, V. Baglio, A. Zaffora, F.D. Franco, M. Santamaria, L. Olivi, S. Pollastri, C. Santoro, Mono-, bi- and tri-metallic platinum group metal-free electrocatalyst for hydrogen evolution reaction following a facile synthetic route, Ind. Chem. Mater. 1 (2023) 343–359, https://doi.org/10.1039/D3IM00058C.

[74] G. Rossi, F. d'Acapito, L. Amidani, F. Boscherini, M. Pedio, Local environment of metal ions in phthalocyanines: K-edge X-ray absorption spectra, Phys. Chem. Chem. Phys. 18 (2016) 23686–23694, https://doi.org/10.1039/C6CP04022E.

[75] H.J. Choi, G. Kwag, S. Kim, Electrochemical and XAFS investigation of nitrite reduction by heat-treated μ-oxo derivative of iron phthalocyanine supported on high area carbon, J. Electroanal. Chem. 508 (2001) 105–114, https://doi.org/10.1016/S0022-0728(01)00523-X.

[76] S.Y. Ha, J. Park, T. Ohta, G. Kwag, S. Kima, In situ iron K-Edge XANES study of iron phthalocyanine irreversibly adsorbed on an electrode surface, Electrochem. Solid-State Lett. 2 (1999) 461, https://doi.org/10.1149/1.1390871.

[77] M.C.M. Alves, J.P. Dodelet, D. Guay, M. Ladouceur, G. Tourillon, Origin of the electrocatalytic properties for oxygen reduction of some heat-treated polyacrylonitrile and phthalocyanine cobalt compounds adsorbed on carbon black as probed by electrochemistry and x-ray absorption spectroscopy, J. Phys. Chem. 96 (1992) 10898–10905, https://doi.org/10.1021/j100205a054.

[78] M. Newville, R. Otten, A. Nelson, T. Stensitzki, A. Ingargiola, D. Allan, A. Fox, F. Carter, Michał, R. Osborn, D. Pustakhod, lneuhaus, S. Weigand, A. Aristov, Glenn, C. Deil, mgunyho, Mark, A.L.R. Hansen, G. Pasquevich, L. Foks, N. Zobrist, O. Frost, Stuermer, azelcer, A. Polloreno, A. Persaud, J.H. Nielsen, M. Pompili, P. Eendebak, lmfit/lmfit-py: 1.2.2, (2023). https://doi.org/10.5281/zenodo.8145703.

[79] Welcome to Python.org, Python.Org. (2023). ⟨https://www.python.org/⟩ (accessed August 10, 2023).

[80] M. Primbs, Y. Sun, A. Roy, D. Malko, A. Mehmood, M.-T. Sougrati, P.-Y. Blanchard, G. Granozzi, T. Kosmala, G. Daniel, P. Atanassov, J. Sharman, C. Durante, A. Kucernak, D. Jones, F. Jaouen, P. Strasser, Establishing reactivity descriptors for platinum group metal (PGM)-free Fe–N–C catalysts for PEM fuel cells, Energy Environ. Sci. 13 (2020) 2480–2500, https://doi.org/10.1039/D0EE01013H.

[81] F. Luo, C.H. Choi, M.J.M. Primbs, W. Ju, S. Li, N.D. Leonard, A. Thomas, F. Jaouen, P. Strasser, Accurate evaluation of active-site density (SD) and turnover frequency (TOF) of PGM-free metal–nitrogen-doped carbon (MNC) electrocatalysts using CO cryo adsorption, ACS Catal. 9 (2019) 4841–4852, https://doi.org/10.1021/acscatal.9b00588.

[82] Q. Zhang, K. Mamtani, D. Jain, U. Ozkan, A. Asthagiri, CO poisoning effects on FeNC and CNx ORR catalysts: a combined experimental–computational study, J. Phys. Chem. C. 120 (2016) 15173–15184, https://doi.org/10.1021/acs.jpcc.6b03933.

[83] S. Brocato, A. Serov, P. Atanassov, pH dependence of catalytic activity for ORR of the non-PGM catalyst derived from heat-treated Fe–phenanthroline, Electrochim. Acta 87 (2013) 361–365, https://doi.org/10.1016/j.electacta.2012.09.053.

[84] W. Zhong, Z. Wang, S. Han, L. Deng, J. Yu, Y. Lin, X. Long, M. Gu, S. Yang, Identifying the active sites of a single atom catalyst with pH-universal oxygen reduction reaction activity, Cell Rep. Phys. Sci. 1 (2020), 100115, https://doi.org/10.1016/j.xcrp.2020.100115.

[85] S. Rojas-Carbonell, K. Artyushkova, A. Serov, C. Santoro, I. Matanovic, P. Atanassov, Effect of pH on the activity of platinum group metal-free catalysts in

oxygen reduction reaction, ACS Catal. 8 (2018) 3041–3053, https://doi.org/10.1021/acscatal.7b03991.

[86] N. Ramaswamy, S. Mukerjee, Fundamental mechanistic understanding of electrocatalysis of oxygen reduction on Pt and non-Pt surfaces: acid versus alkaline media, Adv. Phys. Chem. 2012 (2012) e491604, https://doi.org/10.1155/2012/491604.

[87] R. Sgarbi, K. Kumar, F. Jaouen, A. Zitolo, E.A. Ticianelli, F. Maillard, Oxygen reduction reaction mechanism and kinetics on M-NxCy and M@N-C active sites present in model M-N-C catalysts under alkaline and acidic conditions, J. Solid State Electrochem 25 (2021) 45–56, https://doi.org/10.1007/s10008-019-04436-w.

[88] C. Santoro, K. Artyushkova, S. Babanova, P. Atanassov, I. Ieropoulos, M. Grattieri, P. Cristiani, S. Trasatti, B. Li, A.J. Schuler, Parameters characterization and optimization of activated carbon (AC) cathodes for microbial fuel cell application, Bioresour. Technol. 163 (2014) 54–63, https://doi.org/10.1016/j.biortech.2014.03.091.

[89] K. Artyushkova, S. Rojas-Carbonell, C. Santoro, E. Weiler, A. Serov, R. Awais, R. R. Gokhale, P. Atanassov, Correlations between synthesis and performance of Fe-based PGM-free catalysts in acidic and alkaline media: evolution of surface chemistry and morphology, ACS Appl. Energy Mater. 2 (2019) 5406–5418, https://doi.org/10.1021/acsaem.9b00331.

[90] S. Babanova, K. Artyushkova, Y. Ulyanova, S. Singhal, P. Atanassov, Design of experiments and principal component analysis as approaches for enhancing performance of gas-diffusional air-breathing bilirubin oxidase cathode, J. Power Sources 245 (2014) 389–397, https://doi.org/10.1016/j.jpowsour.2013.06.031.

[91] H. Abdi, L.J. Williams, Principal component analysis, Wiley Interdisciplinary Reviews: Computational Statistics. 2 (2010) 433–459. https://doi.org/10.1002/wics.101.

[92] Q. Ma, H. Jin, J. Zhu, Z. Li, H. Xu, B. Liu, Z. Zhang, J. Ma, S. Mu, Stabilizing Fe–N–C catalysts as model for oxygen reduction reaction, Adv. Sci. 8 (2021), 2102209, https://doi.org/10.1002/advs.202102209.

[93] S. Kabir, K. Artyushkova, A. Serov, B. Kiefer, P. Atanassov, Binding energy shifts for nitrogen-containing graphene-based electrocatalysts – experiments and DFT calculations, Surf. Interface Anal. 48 (2016) 293–300, https://doi.org/10.1002/sia.5935.

[94] L.-N. Lu, Y.-L. Luo, H.-J. Liu, Y.-X. Chen, K. Xiao, Z.-Q. Liu, Multivalent CoSx coupled with N-doped CNTs/Ni as an advanced oxygen electrocatalyst for zinc-air batteries, Chem. Eng. J. 427 (2022), 132041, https://doi.org/10.1016/j.cej.2021.132041.

[95] Y. Chen, I. Matanovic, E. Weiler, P. Atanassov, K. Artyushkova, Mechanism of oxygen reduction reaction on transition metal–nitrogen–carbon catalysts: establishing the role of nitrogen-containing active sites, ACS Appl. Energy Mater. 1 (2018) 5948–5953, https://doi.org/10.1021/acsaem.8b00959.

[96] R. Venegas, C. Zúñiga, J.H. Zagal, A. Toro-Labbé, J.F. Marco, N. Menéndez, K. Muñoz-Becerra, F.J. Recio, Fe3O4 templated pyrolyzed Fe−N−C catalysts. Understanding the role of N-functions and Fe3C on the ORR activity and mechanism, ChemElectroChem 9 (2022), e202200115, https://doi.org/10.1002/celc.202200115.

[97] S. Maldonado, K.J. Stevenson, Influence of nitrogen doping on oxygen reduction electrocatalysis at carbon nanofiber electrodes, J. Phys. Chem. B. 109 (2005) 4707–4716, https://doi.org/10.1021/jp044442z.

[98] J. Lilloja, E. Kibena-Põldsepp, A. Sarapuu, M. Kodali, Y. Chen, T. Asset, M. Käärik, M. Merisalu, P. Paiste, J. Aruväli, A. Treshchalov, M. Rähn, J. Leis, V. Sammelselg, S. Holdcroft, P. Atanassov, K. Tammeveski, Cathode catalysts based on cobalt- and nitrogen-doped nanocarbon composites for anion exchange membrane fuel cells, ACS Appl. Energy Mater. 3 (2020) 5375–5384, https://doi.org/10.1021/acsaem.0c00381.

[99] M.E.M. Buan, A. Cognigni, J.C. Walmsley, N. Muthuswamy, M. Rønning, Active sites for the oxygen reduction reaction in nitrogen-doped carbon nanofibers, Catal. Today 357 (2020) 248–258, https://doi.org/10.1016/j.cattod.2019.01.018.

[100] H. Xie, B. Du, X. Huang, D. Zeng, H. Meng, H. Lin, W. Li, T. Asefa, Y. Meng, High Density Single Fe Atoms on Mesoporous N-Doped Carbons: Noble Metal-Free Electrocatalysts for Oxygen Reduction Reaction in Acidic and Alkaline Media, Small. n/a (n.d.) 2303214. https://doi.org/10.1002/smll.202303214.

[101] S. Hu, W. Ni, D. Yang, C. Ma, J. Zhang, J. Duan, Y. Gao, S. Zhang, Fe3O4 nanoparticles encapsulated in single-atom Fe–N–C towards efficient oxygen reduction reaction: effect of the micro and macro pores, Carbon 162 (2020) 245–255, https://doi.org/10.1016/j.carbon.2020.02.059.

[102] J. Chen, D. Wu, Z. Zhou, Y. Huang, Improved uniformity of Fe3O4 nanoparticles on Fe–N–C nanosheets derived from a 2D covalent organic polymer for oxygen reduction, Int. J. Hydrog. Energy 46 (2021) 27576–27584, https://doi.org/10.1016/j.ijhydene.2021.05.202.